Journal of Power Sources 192 (2009) 231–246

Contents lists available at ScienceDirect

Journal of Power Sources

journal homepage: www.elsevier.com/locate/jpowsour

Review

Progress in understanding and development of $Ba_{0.5}Sr_{0.5}Co_{0.8}Fe_{0.2}O_{3-\delta}$-based cathodes for intermediate-temperature solid-oxide fuel cells: A review

Wei Zhou, Ran Ran, Zongping Shao*

State Key Laboratory of Materials-Oriented Chemical Engineering, College of Chemistry & Chemical Engineering, Nanjing University of Technology, No. 5 Xin Mofan Road, Nanjing 210009, PR China

ARTICLE INFO

Article history:
Received 8 January 2009
Received in revised form 21 February 2009
Accepted 23 February 2009
Available online 6 March 2009

Keywords:
Intermediate-temperature solid-oxide fuel cell
$Ba_{0.5}Sr_{0.5}Co_{0.8}Fe_{0.2}O_{3-\delta}$
Cathode
Oxygen reduction reaction
Perovskite

ABSTRACT

Solid-oxide fuel cells (SOFCs) convert chemical energy directly into electric power in a highly efficient way. Lowering the operating temperature of SOFCs to around 500–800 °C is one of the main goals in current SOFC research. The associated benefits include reducing the difficulties associated with sealing and thermal degradation, allowing the use of low-cost metallic interconnectors and suppressing reactions between the cell components. However, the electrochemical activity of the cathode deteriorates dramatically with decreasing temperature for the typical $La_{0.8}Sr_{0.2}MnO_3$-based electrodes. The cathode becomes the limiting factor in determining the overall cell performance. Therefore, the development of new electrodes with high electrocatalytic activity for oxygen reduction becomes a critical issue for intermediate-temperature (IT)-SOFCs. $Ba_{0.5}Sr_{0.5}Co_{0.8}Fe_{0.2}O_{3-\delta}$ (BSCF) perovskite oxide was first reported as a potential IT-SOFC cathode material in 2004 by Shao and Haile. After that, the BSCF cathode has attracted considerable attention. This paper reviews the current research activities on BSCF-based cathodes for IT-SOFCs. Emphasis will be placed on the understanding and optimization of BSCF-based materials. The issues raised by the BSCF cathode are also presented and analyzed to provide some guidelines in the search for the new generation of cathode materials for IT-SOFCs.

Contents

* Corresponding author. Tel.: +86 25 83172256; fax: +86 25 83172256.
E-mail address: shaozp@njut.edu.cn (Z. Shao).

0378-7753/$ – see front matter © 2009 Elsevier B.V. All rights reserved.
doi:10.1016/j.jpowsour.2009.02.069

1. A general introduction

Fuel cells efficiently convert chemical energy to electricity in a silent and environmentally friendly way. They are a promising alternative to traditional mobile and stationary power sources, such as the internal combustion engine and coal burning power plants. Among the various kinds of fuel cells, solid-oxide fuel cells (SOFCs) have the advantages of the highest energy conversion efficiency and excellent fuel flexibility because of their high operating temperature [1–5]. Although the concept of SOFCs was developed more than a century ago [6–8], they have never received such considerable attention as in the past decades, due to the increasing attention paid by the public for a sustainable development of the world.

Fig. 1 illustrates the operating principles for an SOFC. The typical SOFC single cell consists of three main components, i.e., a porous cathode (or air electrode) and a porous anode (or fuel electrode), sandwiching a dense electrolyte. The distinguishing feature of SOFCs is that the electrolyte is an electronic insulating ion-conducting ceramic that allows only the proton or oxygen ion to pass through. The cathode functions as the electrocatalyst for reduction of oxygen into oxide ions. When an oxygen ionic conducting oxide is adopted as the electrolyte, these ions then diffuse through the solid-oxide electrolyte to the anode, where they electrochemically oxidize the fuel. The released electrons flow through an external circuit to the cathode to complete the circuit and to do work [9]. The efficiency of reversible work converted to electrical work depends on the internal losses in the fuel cell, including the ohmic loss from the electrolyte and the interfacial resistances of the anode and cathode.

Typical SOFCs are based on yttria-stabilized zirconia (YSZ) electrolyte and operated at ~1000 °C [10]. Such a high operating temperature is beneficial for improving the electrode reaction kinetics and reducing the electrolyte ohmic drop. However, it also introduces several serious problems or drawbacks, such as a high possibility of interfacial reaction between the electrode and electrolyte to form insulating phase(s), the densification of the electrode layer due to high-temperature sintering, possible crack formation due to the mismatch of thermal expansion coefficient (TEC) of the cell components, and the requirement of high-cost $LaCrO_3$ as the interconnect material [11].

By contrast, reducing the operating temperature of the SOFCs to an intermediate range, especially less than 650 °C, would have the following advantages:

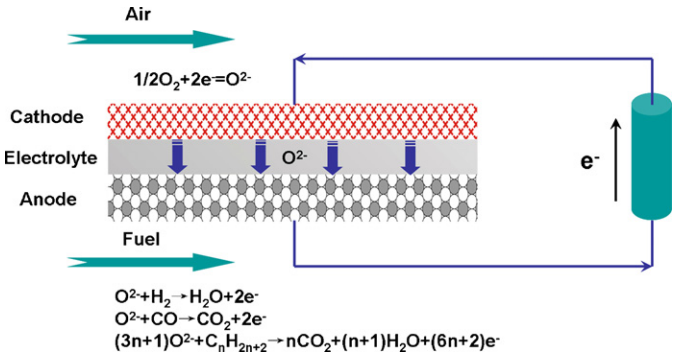

Fig. 1. Schematic of the working principle of a solid-oxide fuel cell.

(a) Offering the choice of low-cost metallic materials, such as stainless steels for the interconnection and construction materials, which makes both the stack and balance-of-plant cheaper and more robust.
(b) Offering the possibility for more rapid start-up and shut-down procedures.
(c) Simplifying the design and material requirements of the balance-of-plant.
(d) Reducing the solid-state reaction between the cell components.

However, it also leads to a significant increase in electrochemical resistance of key cell components, including electrolyte and electrodes. One way to reduce ohmic drop of the cell is to adopt a thin-film electrolyte. With the decrease of membrane thickness, the poor mechanical strength of the thin-film electrolyte suggests that it should be supported on some substrate. Recently, anode or cathode-supported SOFCs have been extensively tested, and some excellent electrochemical performances have been reported [12–23]. Many techniques have been developed for the fabrication of thin-film electrolytes. Will et al. reviewed different thin-film deposition methods for oxides, especially for stabilized zirconia [24]. Recently, Beckel et al. reviewed thin-film (thickness $\leq 1\,\mu m$) deposition techniques and components related to SOFCs, including current research on nanocrystalline thin-film electrolytes and thin-film-based model electrodes [25]. As an alternative way to reduce the ohmic resistance, some materials with higher ionic conductivity have been exploited as the electrolytes for lower temperature SOFCs [26–33]. Kharton et al. reviewed the oxygen ionic conductors reported during the last 10–15 years, including derivatives of c-$Bi_4V_2O_{11}$ (BIMEVOX), $La_2Mo_2O_9$ (LAMOX), $Ln_{10-x}Si_6O_{26}$-based apatites, $(Gd,Ca)_2Ti_2O_{7-\delta}$ pyrochlores, doped CeO_2 fluorites, and perovskite-related phases based on $LaGaO_3$ and $Ba_2In_2O_5$, in order to identify their specific features determining possible applications [34]. Among these materials, the ionic conductivities of ceria-based electrolytes, such as gadolinia-doped ceria (GDC) or lanthanum gallate-based electrolytes, such as $La_{0.8}Sr_{0.2}Ga_{0.8}Mg_{0.2}O_{3-\delta}$ (LSGM) are much higher than that of YSZ, so considerable attention had been focused on these two kinds of materials in the past decades [35–38].

Another large contribution to the significant increase in cell resistance with reducing operating temperature is the increase of electrode polarization resistance, especially from the cathode side [39–42]. The conventional SOFC cathode, strontium-doped lanthanum manganite (LSM), was found to be unsuitable for intermediate-temperature (IT)-SOFCs below 800 °C. Jiang reviewed and updated the development, understanding, and achievements of the LSM-based cathodes for SOFCs [43]. Their structure, non-stoichiometry, defect model, and, in particular, the relation between the microstructure, their properties (electrical, thermal, mechanical, chemical, and interfacial), and electrochemical performance and long-term stability have been critically reviewed. The poor electrochemical activity of LSM cathode was found to be mainly due to its negligible ionic conductivity; therefore, the electrochemical reaction is strictly limited to the triple phase boundary (TPB) [44,45].

To fulfill the intermediate temperature operation of SOFCs, the development of new cathode materials that perform well in this temperature range is then of significant importance. Today, great efforts are being made in the development of novel cathode materials or cathode architecture with improved performance at

reduced temperatures [46–62]. Promising candidates are normally based on mixed oxygen ionic and electronic conducting oxides, such as $Sm_{0.5}Sr_{0.5}CoO_{3-\delta}$ (SSC) and $La_{0.6}Sr_{0.4}Co_{0.2}Fe_{0.8}O_{3-\delta}$ (LSCF) [63–66]. The mixed conductivity extends the active oxygen reduction site from the typical TPB to the entire exposed cathode surface, thus greatly reducing the cathode polarization at low operating temperatures. Polarization mechanisms and modeling of the electrochemical performance on an SOFC cathode have been reviewed by Fleig [67]. The experimental results, particularly measurements using geometrically well-defined LSM cathodes, are discussed. In regard to simulations, the different levels of sophistication used in SOFC electrode modeling studies are summarized and compared. Adler summarized the advances made in understanding of SOFC cathodes since approximately the early 1980s [68]. The review focuses on how new approaches have been used by researchers to better understand cathode mechanisms and how these mechanisms relate to material properties and microstructure. It also attempts to identify ongoing critical questions that will likely be the focus of cathode research and development over the next 10–15 years.

Very recently, Shao and Haile reported a mixed conducting $Ba_{0.5}Sr_{0.5}Co_{0.8}Fe_{0.2}O_{3-\delta}$ (BSCF) oxide as a potential cathode material for $Sm_{0.2}Ce_{0.8}O_{1.9}$ (SDC)-electrolyte-based IT-SOFCs [69,70], which has been extensively applied as the material of ceramic oxygen separation membranes and membrane reactors for partial oxidation of high hydrocarbons to value-added products [71–79]. Very high and promising performance was reported at 600 °C. After that, the application of BSCF as an IT-SOFC cathode material has been attracting considerable attention. Now, it has become one of the hottest cathode materials for IT-SOFCs. This review aims to provide an overview of present research activities in BSCF-based cathodes for IT-SOFCs from applications to oxygen reduction reaction (ORR) mechanisms. Emphasis will be placed on the understanding and development of BSCF-based materials. The problems of the BSCF cathode are also presented and analyzed to provide some guidelines in search for a new generation of cathode materials for IT-SOFCs.

2. Perovskite oxides

Regarding optimization of the cathode materials, there is a general agreement that a fast oxygen exchange reaction between the gaseous oxygen and the lattice oxygen, as well as ionic conductivity in the bulk of the cathode, would be advantageous. These features may be found in some types of oxides, including superconductor materials [80], K_2NiF_4-type oxides [81–83], pyrochlore oxides [84], perovskite oxides [63–66], and perovskite-related oxides, such as A-site ordered double perovskite [85–89], perovskite cuprate structure [90], and perovskite-related intergrowth oxides [91]. Among these types of oxides, perovskite-structured ceramics are the most promising materials of SOFC cathodes due to their high catalytic activity on ORR.

The perovskite oxides have the general formula of ABO_3. The ideal perovskite-type structure has cubic symmetry with space group $Pm3m$. In this structure, the B cation is 6-fold coordinated, and the A cation is 12-fold coordinated, with the oxygen anions. Fig. 2 depicts the corner sharing octahedra that form the skeleton of the structure, in which the center position is occupied by the A cation. Alternatively, this structure can be viewed with the B cation placed in the center of the octahedron and the A cation in the center of the cube. The perovskite structure is thus a superstructure with a ReO_3-type framework built up by the incorporation of A cations into the BO_6 octahedra [92].

In the ideal structure, where the atoms are connecting one another, the B–O distance is equal to $a/2$ (a is the cubic unit cell parameter), while the A–O distance is $(a/\sqrt{2})$ and the following relationship between the ionic radii holds: $r_A + r_O = \sqrt{2}(r_B + r_O)$. Actually, although the equation is not exactly obeyed, some oxides can still retain the cubic structure in ABO_3 compounds. Goldschmidt [93] introduced a tolerance factor (t) to evaluate the deviation from the ideal situation, which is defined by the following equation:

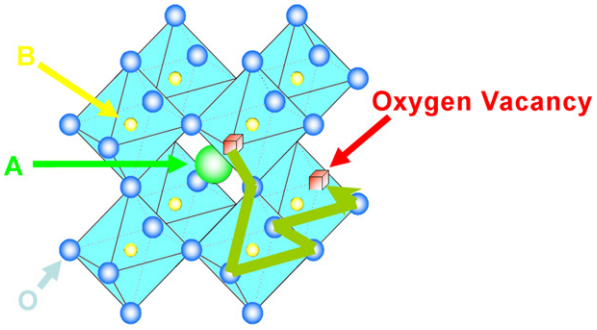

Fig. 2. ABO_3 ideal perovskite structure.

$$t = \frac{(r_A + r_O)}{\sqrt{2}(r_B + r_O)} \quad (1)$$

The value of t is applicable at room temperature to the empirical ionic radii. Although for an ideal perovskite, t is unity, this structure is also found for lower t-values ($0.75 < t < 1.0$). The ideal cubic perovskite structure appears in a few cases for t-values very close to 1 and at high temperatures. In most cases, different distortions of the perovskite structure appear.

Deviations from the ideal structure with orthorhombic, rhombohedral, tetragonal, monoclinic, and triclinic symmetry are known, although the latter three are scarcely and poorly characterized [94–96]. The distorted structure may exist at room temperature, but it can transform to the cubic structure at high temperature. This transition may occur in several steps through intermediate distorted phases. These deviations from the cubic perovskite structure may proceed from a simple distortion of the cubic unit cell, an enlargement of the cubic unit cell, or a combination of both. The deviations are sometimes detrimental to the ionic or electronic conduction, so maintaining the cubic structure of the perovskite oxides is of great importance. Koster and Mertins investigated the crystal structure of BSCF by the X-ray diffraction (XRD). The XRD data could be fitted with a primitive cubic unit cell in space group $Pm3m$ (No. 221), which indicates that BSCF is isomorphous with other cubic perovskites [97].

3. Origination of BSCF

The origination of BSCF can be traced back to $SrCoO_{3-\delta}$ perovskite. $SrCoO_{3-\delta}$ is an important perovskite-type parent compound for the development of a series of functional materials. Depending on the operating temperature, oxygen partial pressure of the environment, thermal history, and synthesis methods, strontium cobaltite may display 2-H type hexagonal perovskite, oxygen vacancy-ordered brownmillerite, rhombohedral perovskite, or cubic perovskite structure [98–102]. Further studies revealed that the phase structure and electrical conductivity of $SrCoO_{3-\delta}$ oxide was closely related to the oxygen content in the composite, which could exhibit a wide range of variation [103]. Among the various phase structures of $SrCoO_{3-\delta}$, the oxide with the cubic phase shows the highest electronic and oxygen ionic conductivity, with a maximum reported total electrical conductivity of ~160 S cm^{-1} at ~950 °C [98]. The derived oxygen ionic conductivity of the cubic phase $SrCoO_{3-\delta}$ based on the permeation flux reached as high as 2.5 S cm^{-1} at 900 °C [98], which is several orders of magnitude

higher than the typical high oxygen ionic conducting electrolyte of YSZ [104]. For the other phases of $SrCoO_{3-\delta}$, the conductivity was substantially lower. The strategy of substitution, either via the A- or B-site, has therefore been extensively applied in order to stabilize the cubic lattice structure of $SrCoO_{3-\delta}$ [105–107].

About two decades ago, Teraoka et al. systematically investigated the general trend of oxygen permeation through ceramic membranes based on doped $SrCoO_{3-\delta}$ oxides with the composition of $Ln_{1-x}A_xCo_{1-y}B_yO_{3-\delta}$ (Ln–La, Pr, Nd, Sm, Gd; A = Sr, Ca, Ba; B = Mn, Cr, Fe, Co, Ni, Cu) [108–110], which is closely related to the oxygen ionic and electronic conductivities of the oxides. The highest oxygen permeation flux was found in the $SrCo_{0.8}Fe_{0.2}O_{3-\delta}$ perovskite, in which the La^{3+} ion was totally substituted by the Sr^{2+} ion. Unfortunately, later examination found that $SrCo_{0.8}Fe_{0.2}O_{3-\delta}$ has only limited mechanical and phase stability [111–113]. Although the doping of metal ion(s) with high valence state (such as La^{3+}) in the A-site of $SrCo_{0.8}Fe_{0.2}O_{3-\delta}$ can lead to the improvement in phase stability of the oxide, the permeability was lowered due to a decrease in oxygen vacancy concentration. Partial substitution of iron in the B-site of $SrCo(Fe)O_{3-\delta}$ by other metal ion(s) has also been attempted [114]; the results showed that the best constitution was still cobaltite ferrites doped with alkaline-earth elements.

As mentioned previously, the phase structure of perovskite is closely related with the Goldschmidt tolerance factor. Since cobalt and iron have multiple oxidation states in perovskite oxide, the tolerance factor can be tuned by varying temperature and oxygen partial pressure. Assuming the most stable oxidation state of 3+ for both cobalt and iron ions, it was found that the A-site cation (Sr^{2+}) of $SrCo_{0.8}Fe_{0.2}O_{3-\delta}$ is too small to sustain a perovskite structure with a cubic symmetry, which was believed to be the most stable lattice symmetry for perovskite [115]. Consequently, Shao adopted a larger sized cation Ba^{2+} to partially substitute Sr^{2+} in order to increase the tolerance factor of the perovskite. Based on Shao's calculation, it was found that substitution of 50% of Sr^{2+} by Ba^{2+} may be the best composition [72]. Thereby, BSCF ($Ba_{0.5}Sr_{0.5}Co_{0.8}Fe_{0.2}O_3$) was proposed as a new material for oxygen separation membranes for oxygen separation from air. Experimental results demonstrated that, indeed, BSCF had better stability than SCF. One significant advantage of applying Ba^{2+} over Ln^{3+} is that the Ba-doped $Sr(Co_{0.8}Fe_{0.2})O_{3-\delta}$ perovskite was thought to possess high oxygen vacancy concentration. As expected, the BSCF membrane showed high oxygen permeation flux and favorable phase stability [71–73].

Later, McIntosh et al. used high temperature XRD (HT-XRD), temperature programmed desorption (TPD), thermogravimetric analysis–differential thermal analysis (TGA/DTA), and neutron diffraction to determine the structure and oxygen stoichiometry of SCF and BSCF up to 1273 K in the P_{O_2} range of 1 to 10^{-5} atm [116]. They found that formation of the vacancy-ordered brownmillerite phase, $SrCo_{0.8}Fe_{0.2}O_{2.5}$, led to zero oxygen release, while no such ordering was observed in the BSCF system by any of the techniques utilized in that work. The oxygen vacancy concentration of BSCF was found to be considerably higher than that of SCF and always higher than that of the ordered brownmillerite phase. The combination of a high vacancy concentration and the absence of the ordering phase may partially account for the higher oxygen permeation fluxes through BSCF membranes in comparison to SCF.

Recently, some studies have proven both experimentally and theoretically that BSCF was also the optimal material in the family of $Ba_xSr_{1-x}Co_yFe_{1-y}O_{3-\delta}$ as a cathode of IT-SOFCs. Wei et al. systematically experimentally characterized $Ba_xSr_{1-x}Co_{0.8}Fe_{0.2}O_{3-\delta}$ ($0.3 \le x \le 0.7$) composite oxides [117]. For $x \le 0.6$ compositions, a cubic perovskite structure was obtained, and the lattice constant increased with increasing Ba content. Large amounts of lattice oxygen were lost below 550 °C, which had a significant impact on thermal and electrical properties. All the dilatometric curves had an inflection between 350 and 500 °C, and thermal expansion coefficients were very high between 50 and 1000 °C, with values larger than 20×10^{-6} K^{-1}. The conductivity was slightly larger than 30 S cm^{-1} above 500 °C, except for $x > 0.5$ compositions. They concluded that $Ba_{0.4}Sr_{0.6}Co_{0.8}Fe_{0.2}O_{3-\delta}$ and BSCF are potential cathode materials.

Chen et al. investigated the influence of iron doping level in $Ba_{0.5}Sr_{0.5}Co_{1-y}Fe_yO_{3-\delta}$ ($y = 0.0$–1.0) oxides on their phase structure, oxygen non-stoichiometry, electrical conductivity, and electrode performance based on symmetrical cell configuration [118]. The increase of the iron doping level resulted in the decrease of the room-temperature oxygen non-stoichiometry and total electrical conductivity and the increase of area specific resistance (ASR) as a cathode on SDC electrolyte. ASR values of 0.085, 0.13, 0.166, 0.3612, and 0.613 Ω cm^2 were observed at 600 °C for $Ba_{0.5}Sr_{0.5}Co_{1-y}Fe_yO_{3-\delta}$ with $y = 0.2$, 0.4, 0.6, 0.8, and 1.0, respectively. A corresponding increase of the activation energy was also observed, with the values of 106.0, 120.2, 121.7, 123.8, and 139.5 kJ mol^{-1} for $y = 0.2$, 0.4, 0.6, 0.8, and 1.0, respectively. The $Ba_{0.5}Sr_{0.5}Co_{1-y}Fe_yO_{3-\delta}$ cathodes at $y = 0.2$ showed the highest electrocatalytic activity for ORR.

Fisher et al. used molecular dynamics simulations to examine the relationship between oxygen ionic conductivity and dopant content in systems with the general formula of $Ba_{1-x}Sr_xCo_{1-y}Fe_yO_{2.5}$, where x and y are varied between 0 and 1 [119]. Results showed that the substitution of Sr by Ba resulted in an increase of the ionic conductivity of the material, with the highest ionic conductivity obtained for $SrFeO_{2.5}$, which agreed well with experimental findings. Calculation of oxygen coordination numbers for each cation species showed that oxygen vacancies tend to cluster around Sr and Co ions, although increased Sr content decreases the tendency towards trapping by drawing vacancies away from the Co ions. The largest amount of trapping (as measured by the deviation from the ideal average coordination numbers of B-site cations) was found to correspond to a minimum in the ionic conductivities at around 50% Fe. The results help to explain why $Ba_{1-x}Sr_xCo_{1-y}Fe_yO_{2-\delta}$ has the high oxide ionic conductivity at $x = 0.5$ and $y = 0.2$.

4. Applications of BSCF as the cathode of IT-SOFCs

4.1. BSCF cathodes on various electrolytes

Shao and Haile were the first to adopt and investigate BSCF as a cathode of SOFCs based on fluorite-type SDC electrolyte [69]. Outstanding performance has been obtained at low temperatures from a single cell based on a 20-μm-thick SDC electrolyte film with humidified (3% water vapor) hydrogen as the fuel and air as the oxidant. Maximum power densities of 1010 and 402 mW cm^{-2} were achieved at 600 and 500 °C, respectively. Subsequently, a considerable interest in BSCF as the cathode material of IT-SOFCs has been received from the research community. Liu et al. [120] reported that by further reducing the thickness of a doped ceria $Gd_{0.1}Ce_{0.9}O_{1.95}$ (GDC) electrolyte to around 10 μm, an anode-supported single cell with the BSCF cathode and a Ni–GDC cermet anode achieved the peak power densities of 1329, 863, 454, 208, and 83 mW cm^{-2} at 600, 550, 500, 450, and 400 °C, respectively. Phase reaction between cathode and electrolyte may become a practical problem for high temperature fuel cells. Wang et al. [121] studied the solid-state reaction between BSCF and SDC by XRD, scanning electron microscope (SEM), and O_2-TPD. Results demonstrated that the phase reaction between BSCF and SDC was negligible, constricted only at the BSCF and SDC interface and throughout the entire cathode with the formation of a new $(Ba,Sr,Sm,Ce)(Co,Fe)O_{3-\delta}$ perovskite phase at firing temperatures of 900, 1000, and ≥1050 °C. It suggests that a firing temperature of ~900 °C is preferred in order to

avoid the interfacial reaction between the BSCF cathode and SDC electrolyte.

LSGM perovskite-type oxide is another electrolyte material with high ionic conductivity at reduced temperatures. Peña-Martínez et al. showed that the BSCF also gives a favorable cathodic performance on an LSGM electrolyte. A single cell with a $La_{0.75}Sr_{0.25}Cr_{0.5}Mn_{0.5}O_{3-\delta}$ (LSCM) anode, a BSCF cathode, and a 1.5-mm-thick LSGM electrolyte delivered a maximum power density of 160 mW cm^{-2} at 800 °C operating on moistened H_2 in the presence of N_2 diluents as fuel and air as oxidant [122].

Protons typically have much lower diffusion activation energy than oxygen ions. Therefore, protonic SOFCs are more promising for lower temperature operation than oxygen ionic SOFCs. Indeed, selected protonic electrolytes, such as doped barium ceria demonstrated very high protonic conductivity at low temperature. However, currently, the poor cathodic performance is the main obstacle for protonic SOFCs to achieve high power output. Lin et al. [123] evaluated the potential application of BSCF as a cathode for a proton-conducting SOFC based on $BaCe_{0.9}Y_{0.1}O_{2.95}$ (BCY) electrolyte. Cation diffusion from BCY to BSCF with the formation of a perovskite-type Ba^{2+}-enriched BSCF and a Ba^{2+}-deficient BCY at a firing temperature as low as 900 °C was observed, with higher firing temperatures leading to larger deviations of the A to B ratio from unity for the perovskites. It was found that the impurity phases did not induce a significant change of the cathodic polarization resistance based on symmetric cell tests; however, the ohmic resistance of the cell obviously increased. Under optimized conditions, a maximum peak power density of ~550 and 100 mW cm^{-2} was reported at 700 and 400 °C, respectively, for the cell with the BSCF cathode fired at 950 °C and a 50 μm BCY electrolyte. The results obtained by Lin et al. were much better than those reported by Peng et al. [124], who applied a BSCF + $BaCe_{0.9}Sm_{0.1}O_{2.95}$ (BCS) composite oxide as the cathode for a proton-conducting BCS electrolyte and a firing temperature of ~1100 °C for fixing the cathode layer to the electrolyte surface. They observed an area-specific polarization resistance of ~2.25 Ω cm^2 at 600 °C; for comparison, Lin et al. reported a value of only 0.5 Ω cm^2 under similar operating conditions. Lin et al. explained that the poor performance reported by Peng et al. could be related to the high firing temperature (1100 °C) and the composite cathode applied. They believed that in the composite cathode, the A-site cation-deficient BCS was formed throughout the electrode layer, which could cover the BSCF surface and considerably block the oxygen reduction over the cathode. In the case of the pure BSCF applied as the cathode layer, the phase reaction occurred only at the interface between the BSCF cathode and the BCY electrolyte; therefore, the oxygen reduction properties of the cathode layer were not seriously affected.

BSCF has also been tried as a cathode on YSZ electrolyte. A strong reaction between BSCF and YSZ was observed at firing temperatures above 900 °C [125,126]. However, a temperature of >900 °C was necessary to obtain the compact attachment of BSCF on the electrolyte. This conflict suggests that the BSCF is hardly applicable directly onto the YSZ electrolyte. Duan et al. studied the chemical compatibility of the BSCF with the GDC electrolyte, as well as that of the GDC with the YSZ electrolyte [126]. BSCF had good compatibility with the GDC electrolyte. The BSCF cathode was adopted for anode-supported YSZ electrolyte cells with and without the application of a 1-μm-thick GDC buffering layer between the cathode and the YSZ electrolyte. The single cells were evaluated by using *I–V* curve measurements and AC impedance spectroscopy. The results showed that a great improvement in cell performance and a significant decrease in polarization resistance were achieved by adding the GDC buffer layer. The optimum firing temperature of the GDC film onto the YSZ film was found to be around 1250 °C, which delivered the maximum power density of 1.56 W cm^{-2} at 800 °C using hydrogen as fuel and air as oxidant. The GDC interlayer was also applied between the BSCF cathode and Sc-stabilized ZrO_2 (ScSZ) electrolyte [127], which resulted in low polarization resistance. It is worth noting that Wang et al. reported that BSCF reacted with GDC at a temperature as low as 850 °C [128]. This may be ascribed to the different fabrication process for the BSCF cathode.

4.2. Synthesis of BSCF powder

The cathode layer in SOFCs is usually fabricated from pre-crystallized powders by any of the methods of spray deposition, screen-printing, or painting, followed by high temperature sintering. Many powder synthesis methods have been applied for the synthesis of cathode materials, such as solid-state reaction, sol–gel, co-precipitation, hydrothermal synthesis, etc. [129–133]. Many studies have shown that the synthesis methods may affect the morphology, conductivity, crystallite size, and surface microstructure of the derived powders [134–138]. Such distinctions could have an evident influence on their properties in application as cathodes for SOFCs. Establishing the relationship between the powder synthesis route and the cathode properties is therefore important for optimizing the cathode performance.

Shao and Haile employed a combined EDTA-citrate (EC) complexing process for the synthesis of BSCF powders [69]. The process was proven to be insensitive to environmental parameters, such as pH and humidity, and capable of large-scale synthesis of powder [139]. Lee et al. synthesized BSCF by the EDTA-citrate method originating from the precursor solutions with different pH values. The BSCF electrode prepared from the precursor solution with a pH value of 8 showed the lowest polarization resistance [140].

Liu and Zhang used a glycine–nitrate process (GNP) to synthesize compositionally uniform BSCF in short firing time [141]. In the GNP process, a saturated aqueous solution containing required amounts of nitrates and glycine was combusted to form ceramic powders. Such a method has the advantages of relatively low-cost, high energy efficiency, fast heating rates, short reaction times, and high compositional homogeneity. The process is also homogeneous because all the reactants are mixed in the solution at the molecular level, resulting in homogeneous reaction products and faster reaction rates. Results showed that the microstructure of as-prepared powders was porous, and their size was less than 20 nm. Pure perovskite phase was completely formed after heat treatment at 850 °C for 2 h in air.

Nano-crystalline BSCF powder has also been successfully synthesized by a novel sol–gel thermolysis method using a combination of PVA and urea by Subramania et al. [142]. It was found that a cubic perovskite BSCF was formed by calcining the precursor at a temperature as low as 450 °C for 5 h. The well-crystalline cubic perovskite BSCF was obtained by calcining the precursor at 650 °C, which was still much lower than that of conventional solid-state reaction methods. In addition, electrical conductivity measurement revealed that the maximum conductivity of 32 S cm^{-1} was obtained in air at 500 °C, comparable to that prepared by other techniques.

In order to demonstrate the significant effect of powder synthesis route on cathodic performance, Zhou et al. synthesized BSCF perovskite by the sol–gel process based on an EC complexing method, nitric acid modified EC route (NEC), and nitric acid-aided EDTA–citrate combustion process (NECC) [143]. Crystallite sizes of 27, 38, and 42 nm were observed for the powders of NECC-BSCF, NEC-BSCF, and EC-BSCF, respectively, calcined at 1000 °C, suggesting a suppressing effect of nitric acid on the crystallite size growth of BSCF [144]. The smaller crystallite size of the powders resulted in a higher degree of sintering of the cathode. An oxygen permeation study of the corresponding membranes demonstrated that nitric acid applied during the powder synthesis had a noticeable detrimental effect on both the oxygen surface exchange kinetics and on

the oxygen bulk diffusion rate of the BSCF oxides. The effect of powder synthesis route on the bulk properties of the oxide was validated by the O_2-TPD technique. Since the oxygen bulk diffusion rate is closely related to the oxygen vacancy concentration, which in turn is closely related to the oxidation state of metal ions in the perovskite structure, a difference in the oxygen bulk diffusion behavior of the various BSCF oxides can be anticipated. On the whole, a decreasing cathodic performance in the sequence of EC-BSCF, NEC-BSCF, and NECC-BSCF was observed. A peak power density of 693 mW cm^{-2} was reported for an anode-supported cell with an EC-BSCF cathode at 600 °C, significantly higher than that with an NEC-BSCF cathode (571 mW cm^{-2}) or an NECC-BSCF cathode (543 mW cm^{-2}) under similar operation conditions.

Recently, the formation process of BSCF synthesized by EDTA-citrate was investigated in detail by Martynczuk et al. using advanced modern techniques [145], such as transmission electron microscopy (TEM), energy-filtered transmission electron microscopy (EFTEM), and energy-loss near-edge structures (EELS). Their results indicated that the perovskite structure is formed in a nanometer-scale solid-state reaction between a spinel-$(Fe_{0.6}Co_{0.4})Co_2O_4$ and carbonate-$(Ba_{0.5}Sr_{0.5})CO_3$ in the aragonite polymorph,

$$3(Ba_{0.5}Sr_{0.5})CO_{3(s)} + (Fe_{0.6}Co_{0.4})Co_2O_{4(s)} \xrightarrow{O_2} 3(Ba_{0.5}Sr_{0.5})(Fe_{0.2}Co_{0.8})O_{3-\delta(s)} + 3CO_{2(g)} \quad (2)$$

Grains obtained in different perovskite synthesis steps showed that the primarily formed perovskite crystals are of the same size as the intermediates and coarsen afterwards during the thermal treatment. The common calcination temperature of 950 °C can be decreased to 750 °C to avoid over-sintering and therefore to facilitate the firing of BSCF to electrolyte. This profound knowledge of the BSCF perovskite formation process opens new ways to engage the microstructure of the underlying ceramic material, for example, to fine-tune both grain stoichiometry and grain boundaries in the ceramic material.

4.3. Morphology of the cathode

Another key issue related to the cathodic performance is the electrode microstructure. The pore size, morphology, and electrode porosity of the cathode govern the transport of gaseous species through the electrodes, affecting the electrode performance [146]. Today, the electrodes are commonly deposited by screen-printing on the electrolyte, and the porosity is controlled using pore formers, which are generally organic compounds and/or graphite [147,148]. However, it is difficult to control the pore distribution using this method, giving rise to microstructures with non-uniform geometry and low specific surface areas. A precise control of the porosity and a larger specific surface area of the electrode may improve the cell performance as a result of an increase in the concentration of active sites for ORR.

Mamak et al. synthesized mesoporous (nickel/platinum) YSZ materials by a soft chemistry self-assembly strategy [149]. The approach was based on the co-assembly of a supramolecular cationic surfactant template: YSZ glycolate and nickel (II) or platinum (IV) complexes. This synthetic strategy yielded compositionally homogeneous mesoporous YSZ, where nanoscale nickel oxide or platinum metal clusters were uniformly dispersed throughout the material. Upon calcination of the as-synthesized material, the surfactant template was removed, and a reconstructive structural transformation occurred and led to a porous material with nanocrystalline YSZ channel walls, a narrow pore size distribution, and high surface areas, which could lead to significant improvements in fuel/oxidant mass transport, oxide ion mobility, electronic conductivity, and charge transfer at the TPB region of SOFC electrodes.

Porous materials with high relative surface area can also be obtained by using a colloidal crystal templating method [150–157]. In this case, a colloidal crystal template was prepared via a regular arrangement of organic microspheres (e.g., polymethyl methacrylate, PMMA). Chi et al. synthesized a porous $La_{0.7}Ca_{0.3}MnO_3$ (LCMO) material using PMMA spheres as a template [150]. This porous network is composed of nanometer-sized LCMO wires with highly ordered spherical voids. Sadakane et al. presented a facile procedure to produce three-dimensionally ordered macroporous (3DOM) perovskite-type $La_{1-x}Sr_xFeO_3$ mixed metal oxide using PMMA as the template, which did not need any pre-synthesis of the alkoxide precursors [151]. The 3DOM perovskite-type materials showed higher catalytic activity for combustion of nanosized carbon.

Recently, PMMA was also used as the template to fabricate the 3DOM cathode for SOFCs. Ruiz-Morales et al. [152] have recently reported that the performance of a cell with YSZ electrolyte, LSM–YSZ composite as the cathode, and NiO–YSZ as the anode was improved by up to 30% by using a combination of nanometric oxide powders and PMMA as a pore former to control the porosity of the electrodes. Zhang et al. prepared dual-scale porous electrodes for SOFCs using PMMA foam as the template [153]. After removing the template at 800 °C, the porous cathode was obtained. The electrode consisted of regularly distributed cellular pores with 1 μm diameters. The interconnected walls were approximately 0.5–1-μm-thick. The primary particles of the composite were about 100 nm in diameter. The $Sm_{0.5}Sr_{0.5}CoO_{3-\delta}$-GDC cathode showed an ASR of 0.39 Ω cm^2 at 750 °C. However, this method was only applicable when the starting oxide powders had a particle size in the nanometer range. Furthermore, the high firing temperatures required to ensure good contact between particles caused a significant decrease in the specific surface area of the starting nanoparticles due to particle agglomeration and sintering.

Ruiz-Morales et al. successfully prepared 3DOM BSCF and BSCF-YSZ cathodes using PMMA as the template [152]. Moreover, the particle size of BSCF was ~200 nm versus ~2 μm prepared by the traditional method. However, the electrochemical performance of these 3DOM BSCF-based cathodes has not been reported. This opens a new direction for the optimization of the BSCF cathode. It is worth noting that the porosity should be deliberately controlled. Excessive high porosity may decrease the electrocatalytic activity of the BSCF cathode because of the low electronic conductivity of BSCF.

4.4. In the application of single-chamber SOFCs

One difficulty associated with high-temperature fuel cells is the sealing. Failure to obtain a gas-tight seal between chambers is very serious, causing gas leakage and eventual destruction of the stacked cells. One approach towards addressing the above challenge is to design SOFCs with only one gas chamber. This type of SOFCs is called a single-chamber SOFC (SC-SOFC), in which both the anode and cathode are exposed to the same mixture of fuel and oxidant gas. As a result, the gas-sealing problem can be inherently avoided, since no separation between fuel and air is required. In addition, carbon deposition is less of a problem due to the presence of a large amount of oxygen in the mixture [158]. The operating principle of a SC-SOFC is based on the different catalytic activity and selectivity of the anode and cathode towards the fuel-air mixture. The BSCF cathode also showed very promising performance in the SC-SOFC application for its high electrochemical catalytic activity for oxygen reduction and poor activity for fuel oxidation [69,70,159–161]. It was reported that a peak power density of 358 mW cm^{-2} was observed at a furnace temperature of 525 °C when the BSCF cathode was operated in a single-chamber mode

using a propane/oxygen/He mixture at a 4:9:36 volumetric ratio as the feed gas [69]. Significant further improvement in the power density was observed by incorporating 30 wt% SDC into the BSCF cathode; a peak power density of 440 mW cm^{-2} was reached at a furnace temperature of 500 °C [69]. After that, Shao et al. reported that, under optimized conditions, a peak power density as high as 760 mW cm^{-2} was obtained for a thin-film electrolyte fuel cell with a Ni/SDC anode and a BSCF/SDC (70:30 wt%) cathode operated on a methane–oxygen–helium stream, comparable to what typically can be obtained in a dual-chamber fuel cell by applying methane fuel [159,160].

Zhang et al. investigated the initialization process of a NiO/SDC anode-supported single-chamber SOFC with a BSCF/SDC cathode [161]. In situ initialization by hydrogen led to simultaneous reduction of both the anode and cathode; however, the cell still delivered a maximum power density of ~350 mW cm^{-2}, attributed to the partial re-formation of the BSCF phase under the methane–air atmosphere at high temperatures. It is worth noting that the oxygen ion conductivity of BSCF is, in fact, higher than that of SDC. It is for this reason that the introduction of a small amount of the electrolyte material could decrease cathode performance in a dual-chamber configuration, rather than increasing it [69]. However, incorporation of electrolyte material into the BSCF cathode under the single-chamber fuel-cell configuration improved performance, and it is likely that the electrolyte is beneficial for limiting the detrimental influence of in situ generated CO_2 on the oxygen surface exchange kinetics of BSCF. The significant impact of CO_2 on the electrochemical performance of the BSCF cathode will be discussed later.

5. Fundamental understanding of BSCF

5.1. Mass and charge transport in mixed conducting oxides

To get a better understanding of the extremely high electrochemical performance of the BSCF cathode at intermediate temperatures, the basic knowledge of oxygen reduction processes on the cathode should first be understood [162]. When a gradient of the electrochemical potential is unequal to zero, a net particle flux, J, can be given by

$$J_i = -\frac{\sigma_i}{z_i^2 e^2}\nabla\tilde{\mu}_i. \quad (3)$$

Here, σ is the electrical conductivity. Eq. (3) is the fundamental transport equation, which can be derived within the framework of linear irreversible thermodynamics. Well-known special cases of Eq. (3) are Ohm's law (for $\nabla\mu = 0$) and Fick's law of diffusion (for $\nabla\varphi = 0$ and $a_i = c_i$). These relationships have a wide validity range, showing that the linear approximation is often a good description for transport phenomena in ionic solids. The electrical conductivity, σ_i, is proportional to the concentration, c_i, and the mobility, u_i, of particles i:

$$\sigma_i = |z_i| e u_i c_i \quad (4)$$

When transport processes in solid compounds are considered, one particular type of particle is frequently much more mobile than the other(s). In such cases, the partial lattice of the virtually immobile type of particle is chosen as the reference system. For a mixed conducting material, the total conductivity, σ_{tot}, can be written as the sum over the partial conductivities of all electronic (eon) and ionic (ion) defects, provided that the charge carriers are transported independently of each other. In most cases, this is a good approximation.

$$\sigma_{tot} = \sigma_{eon} + \sigma_{ion} = \sum_i |z_{i,eon}| e u_{i,eon} c_{i,eon} + \sum_j |z_{j,ion}| e u_{j,ion} c_{j,ion} \quad (5)$$

Table 1
Elementary step in the cathodic oxygen reduction reaction on a mixed conducting electrode material [162].

Rank	Reaction step
1	Diffusion of O_2 molecules in the gas phase to the electrode
2	Adsorption of O_2 on the surface of the electrode
3	Dissociation of molecular into atomic oxygen species
4	Charge transfer from the electrode to oxygen species before or after dissociation
5	Incorporation of oxide ions into vacancies in the crystal lattice of the electrode
6	Bulk transport of O^{2-} ions through the electrode to the electrode/electrolyte interface
7	Transfer of O^{2-} ions across the electrode/electrolyte interface

The total conductivity is typically determined by either the electronic or the ionic term. A material that exhibits both electronic and ionic conductivity is referred to as mixed ionic electronic conductor (MIEC), although this term is not strictly defined in the literature. A general way to obtain materials with high ionic conductivity is to increase their vacancy concentration. A combined in situ neutron diffraction and thermogravimetric study [163] yielded unusually high values for the oxygen non-stoichiometry in BSCF of $\delta = 0.7$–0.8 between 600 and 900 °C in the P_{O_2} range of 10^5–10^2 Pa, as shown in Fig. 3. Exceptionally high concentrations of mobile oxygen vacancies accompanied by excellent phase stability are accountable for the large oxygen transport rates of BSCF.

5.2. Electrochemical processes at solid-oxide fuel cell (SOFC) cathodes

The sum reaction at the cathode can be expressed by the following formula:

$$O_2 + 4e^- \rightarrow 2O^{2-} \quad (6)$$

However, this reaction is actually quite complex and comprises a number of elemental steps, such as diffusion, adsorption, dissociation, ionization, and finally, incorporation of oxygen into the crystal lattice of the electrolyte. In general, there are two reaction mechanisms: the surface and the bulk path. If the electrode material is a pure electronic conductor (e.g., Pt), the surface path is the only possible mechanism [164]. In this case, oxygen molecules from the gas phase adsorb onto the surface and diffuse to TPB, where O^{2-} incorporates into the vacancies of the electrolyte. In another case, if the electrode material itself is an oxygen ionic conductor, an alternative reaction path becomes possible. By introducing bulk ionic transport, oxygen can be reduced to O^{2-} over a significant portion of the electrode surface, thereby extending the size of the active region and improving the kinetics at reduced temperatures.

5.3. Oxygen surface exchange and bulk diffusion in BSCF

In multistep chemical reactions, the reaction rate of one particular step is often much lower than those of all other serial processes involved. The kinetics is then determined by this "slow" process only, while all others are "fast", i.e., in equilibrium. Table 1 lists reaction steps to be considered as potentially rate limiting for the case of a mixed conducting electrode material [162]. Quantitatively, oxygen surface exchange and bulk diffusion are frequently expressed by effective rate constants: k (for oxygen surface exchange) and D (for oxygen bulk diffusion); k essentially comprises the four surface-related steps in Table 1 (steps 2–5), while D (step 6) is related to the ionic conductivity of the material. Both high k and D values are generally considered necessary for an appreciable performance of a cathode material.

Shao and Haile calculated the oxygen diffusion and surface exchange coefficients at different temperatures from the depen-

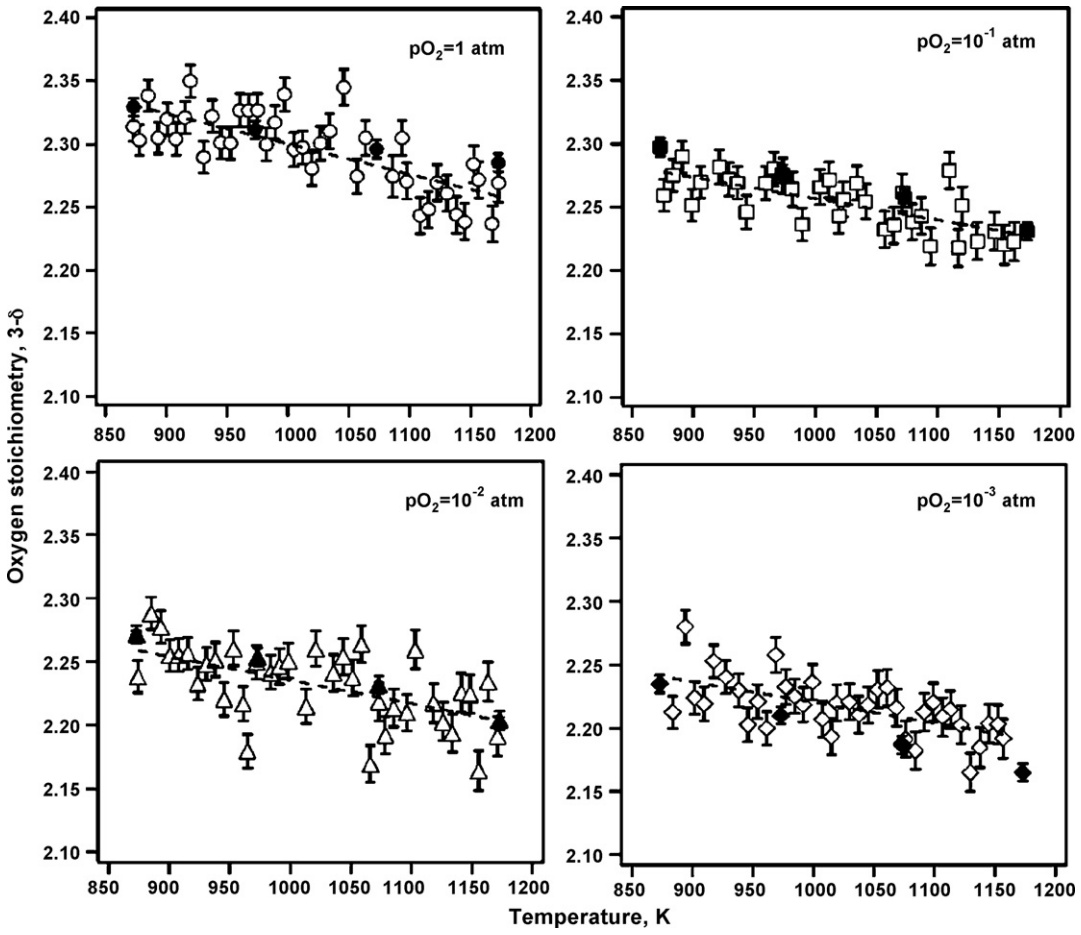

Fig. 3. Oxygen stoichiometry versus temperature as a function of oxygen partial pressure for BSCF measured by neutron diffraction (open symbols) and thermogravimetric analysis (closed symbols). Dashed lines are linear fits to the neutron diffraction data [163].

dence of oxygen permeation flux on the oxygen partial pressure term based on the surface current exchange model [69]. The oxygen flux across a mixed oxygen ion and electron conductor, in which electronic conductivity dominates the total conductivity and in which the Nernst–Einstein relationship accurately describes the relationship between ionic conductivity and ion diffusivity, is given by

$$J_{O_2} = \frac{D_V}{2L}(C''^{,s}_V - C'^{,s}_V) \tag{7}$$

where D_v is the oxygen diffusion coefficient, L is the thickness of the membrane, and C^s_V is the oxygen vacancy concentration at the surface, with $''$ indicating the oxygen-lean side and $'$ indicating the oxygen-rich side. For materials in which both surface exchange kinetics and bulk ion diffusion contribute to limiting the overall mass flux process, the surface vacancy concentration is not known a priori. It can be shown, however, under the reasonable assumption that the concentration of electronic species is constant across the membrane (i.e., no voltage is generated) that the flux under the conditions of mixed control is given by

$$J_{O_2} = \frac{D_V}{2L}\left[\frac{1}{1+(D_V/2Lk_a)(P'^{,-0.5}_{O_2}+P''^{,-0.5}_{O_2})}\right](C''^{,e}_V - C'^{,e}_V) \tag{8}$$

where k_a is the surface exchange coefficient, P_{O_2} is the oxygen partial pressure, C^s_V is the oxygen vacancy concentration at the surface under equilibrium conditions, and $''$ and $'$ again indicate the oxygen-lean and oxygen-rich sides of the membrane. This second equation can be rewritten as

$$\frac{(C''^{,e}_V - C'^{,e}_V)}{J_{O_2}} = \frac{2L}{D_V} + \frac{1}{k_a}(P'^{,-0.5}_{O_2} + P''^{,-0.5}_{O_2}) \tag{9}$$

and thus, a plot of $(C''^{,e}_V - C'^{,e}_V)/J_{O_2}$ versus $1/P'^{,0.5}_{O_2} + 1/P''^{,0.5}_{O_2}$ yields $2L/D_v$ as the intercept and $1/k_a$ as the slope. The surface exchange coefficient of 3×10^{-2} cm^2 s^{-1} atm$^{-0.5}$ and oxygen vacancy diffusion rate of 7.3×10^{-5} cm^2 s^{-1} at 775 °C and 1.3×10^{-4} cm^2 s^{-1} at 900 °C were derived, which are 2–200 times greater than those of comparable cathode perovskites.

Baumann et al. investigated the electrochemical properties of geometrically well-defined BSCF microelectrodes by impedance spectroscopy [165]. The microelectrodes of 20–100 μm diameter and 100 nm thickness were prepared by pulsed laser deposition (PLD), photolithography, and argon ion beam etching. The ORR at these model electrodes is limited by interfacial processes, i.e., by the oxygen surface exchange and/or by the transfer of oxide ions across the electrode/electrolyte boundary, whereas the resistance associated with the transport of oxide ions through the bulk of the thin-film electrode is negligible. The experiments revealed an extremely low absolute value of the electrochemical surface exchange resistance of only 0.09 (±0.03) Ω cm^2 at 750 °C in air, which is more than a factor of 50 lower than the corresponding value measured for $La_{0.6}Sr_{0.4}Co_{0.8}Fe_{0.2}O_{3-\delta}$ microelectrodes with the same geometry [166]. The quantity R_s can be converted into an effective surface exchange rate constant, k^q, according to [167]

$$k^q = \frac{kT}{4e^2R_sc_O}, \tag{10}$$

where k is Boltzmann's constant, T is the absolute temperature, e is the elementary charge, R_s is the area-specific surface resistance, and c_O is the concentration of lattice oxygen. The superscript q denotes the determination via an experiment in which an electrical driving force is applied to the sample. Using crystallographic and non-stoichiometry data from Ref. [163] to calculate c_O, one obtains for BSCF an effective surface exchange rate constant of $k_q = 5 \times 10^{-5}$ cm s^{-1} at 750 °C in air.

Bucher et al. studied the oxygen exchange kinetics of BSCF by electrical conductivity relaxation as a function of temperature in the range 550–725 °C with chemical diffusion coefficients $D_{chem} = 1 \times 10^{-6}$ to 3×10^{-5} cm^2 s^{-1} and surface exchange coefficients $k_{chem} = 2 \times 10^{-4}$ to 3×10^{-3} cm s^{-1} [168]. The activation energies of the kinetic parameters amount to $E_a(D_{chem}) = 86 \pm 8$ kJ mol^{-1} and $E_a(k_{chem}) = 64 \pm 12$ kJ mol^{-1}. Furthermore, the ionic conductivity was obtained according to the Nernst–Einstein relation [169]:

$$\sigma_O = \frac{4F^2(3-\delta)D_O}{RTV_m}, \quad (11)$$

where $V_m = 38.3 \pm 0.3$ cm^3 mol^{-1} was used as the mean molar volume. The calculated ionic conductivities amount to $\sigma_{ion} = 0.006 \pm 0.002$ S cm^{-1} (600 °C) and $\sigma_{ion} = 0.018 \pm 0.008$ S cm^{-1} (700 °C).

Both the high oxygen ionic conductivity and surface exchange coefficient allow the oxygen incorporation to occur over the whole surface of BSCF, which dramatically improves the effective zone for ORR.

5.4. Rate-determining step in ORR on BSCF cathode operated below 600 °C

The BSCF cathode has shown favorable performance at 600 °C. However, ASRs of ~0.17 and ~0.6 Ω cm^2 were obtained for a BSCF cathode at 550 and 500 °C, respectively [69], which are still higher than the target value of 0.15 Ω cm^2 for a cathode, as pointed out by Steele [170]. To further reduce the polarization resistance at temperatures <600 °C, the rate-determining step should be determined.

Fleig and Maier studied the effects of the ionic conductivity and the surface reaction coefficient on the polarization of mixed conducting cathodes by multi-dimensional finite element simulations [171]. Depending on the ratio of k^q/D^q of a mixed conducting cathode, four regimes can be distinguished (shown in Fig. 4):

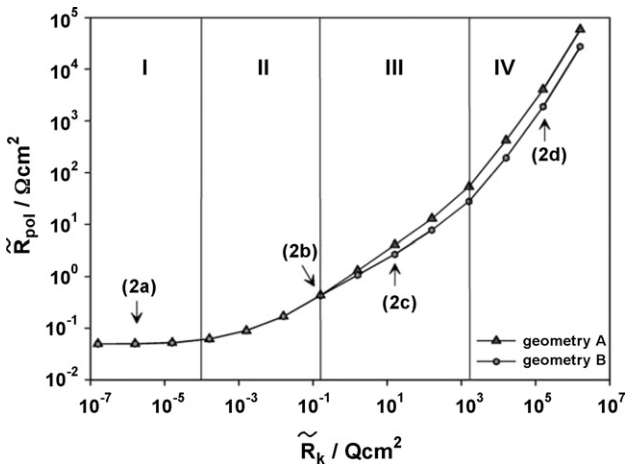

Fig. 4. Area-related polarization resistance for different R_k (resistance of surface reaction)-values and two geometries; $L_p = 1.6$ μm, $\sigma_{ion} = 10^{-3}$ S cm^{-1}. Four different regimes (I–IV) can be distinguished. Increasing R_k leads to a decreasing density of equipotential lines [171].

Regime I: For k^q/D^q values much larger than the inverse particle size L_p, only small regions close to the three phase boundaries are relevant with respect to oxygen reduction.
Regime II: A decreasing k^q/D^q ratio "activates" progressively more of the cathode; i.e., the area of the MIEC surface involved in the ORR monotonically increases; in regime II ($L_p k^q/D^q$ values between 1 and 1000), it is still mainly the first particle layer that contributes to the oxygen reduction.
Regime III: $k^q L_p/D^q$ values <1 lead to a penetration of the ionic current into the cathode network.
Regime IV: The entire cathode surface is of importance ($k^q L_p/D^q$ values $\ll 1$).

For the BSCF cathode, the average size of BSCF particles is ~2 μm [172], k^q is 2×10^{-4} cm s^{-1}, and D^q is 1×10^{-6} cm^2 s^{-1} at 550 °C [168]; thus, the value of $L_p k^q/D^q$ is ~0.04. This indicates that the oxygen reduction can occur on the overall surface of BSCF at this temperature (*Regime IV*). In such a regime, the polarization resistance of the cathode is dramatically influenced by the oxygen surface reaction. Therefore, the optimization of the surface is expected to further reduce the polarization resistance of the BSCF cathode.

6. Optimization of the BSCF cathode

To properly function as a cathode in an SOFC, the material should have a high electrocatalytic activity towards oxygen reduction as well as a high chemical stability in an oxidizing environment without the formation of highly resistive reaction products with the electrolyte and current collector. Furthermore, the material should exhibit similar thermo-mechanical properties as the electrolyte to prevent stresses from developing upon heating and cooling, and it should have high electrical conductivity [173]. The progress of the optimization of the BSCF cathode has been made by Shao et al., as summarized in Table 2.

6.1. Enhancement of ORR on the BSCF

6.1.1. BSCF-electrolyte composite cathode

It has been generally considered that composite electrodes, which typically consist of a mixed oxygen ionic, an electronic conducting material, and an ionic conductor, exhibit higher performance than pure-phase electrodes. Several composite cathodes, like LSM–YSZ [44,174], SSC–SDC [175], and LSCF–GDC [66,176], have been extensively studied with proven improvement of electrochemical properties. For that reason, the BSCF-SDC [121,177,178], BSCF-LSGM [179], and BSCF-$BaZr_{0.1}Ce_{0.7}Y_{0.2}O_3$ (BZCY) [180] composite cathodes have been studied by some groups.

Wang et al. [121] examined the properties and performance of BSCF/SDC (70:30 in weight ratio) composite cathode prepared by mechanical mixing for IT-SOFC. The BSCF/SDC composite demonstrated modestly better performance than the pure BSCF cathode at a firing temperature of 1000 °C. However, it showed worse performance than BSCF at other temperatures. Even when fired at 1000 °C, the increase in cathode performance with the SDC addition was very limited for the BSCF/SDC cathode. An ASR of about 0.099 Ω cm^2 was observed for a pure BSCF cathode, while it was about 0.064 Ω cm^2 for a BSCF/SDC composite cathode, an improvement of only ~36%. For SSC, LSM, and LSCF, the formation of a composite cathode by the introduction of ionic conducting phase resulted in the improvement of the cathode performance by more than one order of magnitude [174,175,66,176]. Such improvement was due to the extension of the active oxygen reduction sites from the traditional TPB to the entire cathode layer. Since the BSCF by itself is a mixed conducting oxide with the oxygen ionic conductiv-

Table 2
The progress on the electrochemical performance of the BSCF-based cathodes reported by Shao et al.

Cathode	Electrolyte	Firing temperature (°C)	Operating temperature (°C)	ASR ($\Omega\,cm^2$)	Ref.
BSCF	SDC	1000	600 550	0.07 0.19	[69]
BSCF + SDC	SDC	1000	600 550	0.064 0.17	[121]
BSCF + SDC/BSCF + SDC + Ag	SDC	1000/800[a]	600	0.07	[196]
BSCF + LC (50 vol.%) BSCF + LC (30 vol.%)	SDC SDC	950 950	600 600	0.43 0.21	[189]
$Ba_{0.5}Sr_{0.5}(Co_{0.8}Fe_{0.2})_{0.97}O_{3-\delta}$	SDC	1000	600 550	0.069 0.181	[187]
$Ba_{0.5}Sr_{0.5}(Co_{0.8}Fe_{0.2})_{0.83}O_{3-\delta}$	SDC	1000	600 550	2.08 5.73	[187]
$(Ba_{0.5}Sr_{0.5})_{0.97}Co_{0.8}Fe_{0.2}O_{3-\delta}$	SDC	1000	600 550	0.138 0.396	[202]
$(Ba_{0.5}Sr_{0.5})_{0.80}Co_{0.8}Fe_{0.2}O_{3-\delta}$	SDC	1000	600 550	0.270 0.838	[202]
BSCF + Ag(reduced by N_2H_4)	SDC	1000/850[a]	600 550	0.038 0.070	[193,213]
BSCF + Ag(reduced by HCHO)	SDC	1000/850[a]	600 550	0.171 0.661	[193,213]
BSCF	BCY	900	750 600	0.04 0.5	[124]
		1000	750 600	0.058 0.62	[124]

[a] The firing temperature of Ag.

ity even higher than SDC [69], only slightly better performance for the BSCF/SDC cathode as compared with the pure BSCF was unlikely to have been contributed by the oxygen ionic conductivity of SDC. It was ascribed to the enlarged cathode surface area contributed by the fine SDC particles [121].

6.1.2. Surface modification

Even though a high oxygen surface exchange coefficient can be obtained for BSCF as compared with other MIEC cathodes, such as LSCF and SSC [181], the oxygen surface processes are still the RDS of ORR compared to its even higher oxygen bulk diffusion rate. The oxygen permeation study of the BSCF demonstrated that the permeation rate was mainly rate-determined by the relatively slow surface exchange kinetics at the oxygen lean side (or reaction side) membrane surface [182]. In general, improving oxygen vacancy concentration and/or electronic conductivity can promote the oxygen surface exchange. Both aspects were studied to improve the cathode performance.

Typically in perovskite oxides ABO_3, the ratio of A-site cation to B-site cation is unity. However, it was found that the perovskite lattice structure could still be sustained when the A/B ratio is different from unity for some perovskite oxides, such as LSCF oxide [183–186]. In order to introduce additional oxygen vacancy into BSCF lattice, Zhou et al. synthesized and investigated cation non-stoichiometric $Ba_{0.5}Sr_{0.5}(Co_{0.8}Fe_{0.2})_{1-x}O_{3-\delta}$ ($BS(CF)_{1-x}$) oxides as cathodes for IT-SOFCs [187]. The B-site cation deficiency in $BS(CF)_{1-x}$ resulted in lattice expansion and the creation of more active sites for ORR due to the lowered valence states of the B-site ions and the increased oxygen vacancy concentration, which improved the oxygen adsorption process. It is interesting that the B-site deficiency does not promote charge compensation by elevating the valence state of the B-site cations [188]. These phenomena can be explained by the defect chemical incorporation reactions as follows:

$$BaO \rightarrow Ba_A + V''''_B + O_O^{\times} + 2V_O^{\bullet\bullet} \quad (12)$$

The increase in lattice constant would result, in part, from the fact that Ba^{2+} has a larger ionic radius than Sr^{2+}. On the other hand, since the initial oxidation state on the B-site is not actually 4+, one cation vacancy on the B-site would not exactly provide charge balance for the two oxygen vacancies. Therefore, a complete charge balance would require that some of the B-site cations lower their valences. On the other hand, the B-site cation deficiency could also result in higher resistances for oxygen adsorption (due to the formation of BaO and/or SrO impurities), and oxygen-ion transfer (by facilitating the solid-phase reaction between the cathode and the electrolyte). By taking all these factors into account, $BS(CF)_{0.97}$ was the optimal composition, which leads to a peak power density of $1026.2 \pm 12.7\,mW\,cm^{-2}$ at 650 °C for a single cell. The ORR mechanism on the A-site excessive barium strontium cobalt ferrites cathode is proposed and shown in Fig. 5.

It is generally accepted that an ideal SOFC cathode should possess high electronic conductivity ($100\,S\,cm^{-1}$) at the desired operating temperatures. The relatively low electronic conductivity of BSCF ($\sim 40\,S\,cm^{-1}$ in air) seems to be one of the key problems with respect to the relatively low electrochemical performance at low temperature. In order to increase the electronic conductivity of the electrode, we can introduce a high electrical conducting phase, such as an oxide or a metal phase. A novel BSCF+ $LaCoO_3$ (LC) composite oxide was first developed for the potential application as a cathode for IT-SOFC by Zhou et al. [189]. LC oxide was reported to have a maximum electrical conductivity of $\sim 1000\,S\,cm^{-1}$ [190], about 20 times that of BSCF. X-ray diffraction examination demonstrated that the solid-state reaction between LC and BSCF phases occurred at temperatures above 950 °C and formed the final product with the composition of $La_{0.316}Ba_{0.342}Sr_{0.342}Co_{0.863}Fe_{0.137}O_{3-\delta}$ at 1100 °C. The inter-diffusion between BSCF and LC was identified by the environmental scanning electron microscopy and energy dispersive X-ray examination. The electrical conductivity of the BSCF/LC composite oxide increased with increasing calcination temperature and reached a maximum value of $\sim 300\,S\,cm^{-1}$ at a calcination temperature of 1050 °C, while the electrical conductivity of the pure BSCF was only $\sim 40\,S\,cm^{-1}$. The improved conductiv-

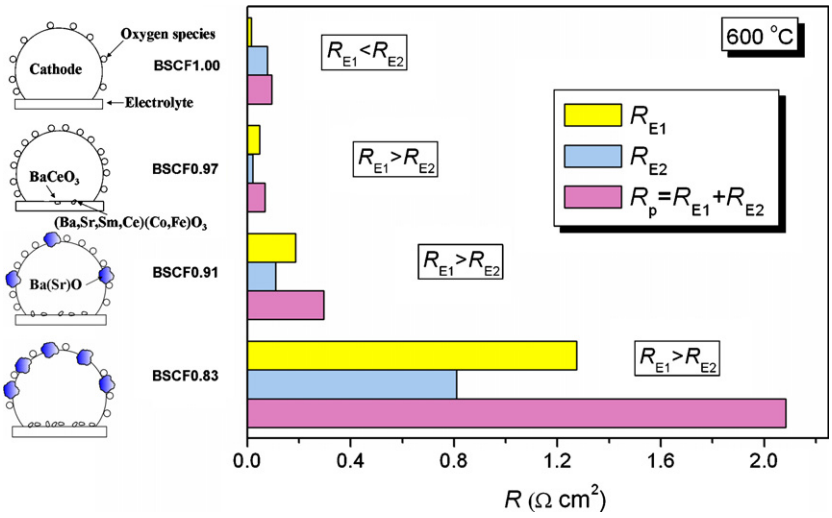

Fig. 5. Mechanism for A-site excess barium strontium cobalt ferrites as the cathode [187].

ity resulted in an attractive cathodic performance of the BSCF/LC composite. An area-specific resistance as low as 0.21 $\Omega\,cm^2$ was achieved at 600 °C for the BSCF (70 vol.%) + LC (30 vol.%) composite cathode calcined at 950 °C for 5 h. Peak power densities as high as ~700 mW cm^{-2} at 650 °C and ~525 mW cm^{-2} at 600 °C were reached for the thin-film fuel cells with the optimized cathode composition and calcination temperatures. Similar results were also observed by using SSC or LSM as a promoter [191,192].

To avoid the solid-state reaction between BSCF and the second oxide phase in the composite cathode, Ag was applied as the electronic conducting phase to replace the oxide conductor. Silver-modified BSCF cathodes were first prepared by an electroless deposition process using N_2H_4 as the reducing agent at room temperature by Zhou et al. [193]. This fabrication technique, together with tailored electrode porosity, modified the BSCF electrodes with silver content that varied from 0.3 to 30 wt% without damaging the electrode microstructure. Both the Ag loading and firing temperatures were found to have a significant impact on the electrode performance, which could facilitate or block the electrochemical processes of the BSCF-based cathodes, processes that include charge-transfer, oxygen adsorption, and oxygen electrochemical reduction. At an optimal Ag loading of 3.0 wt% and firing temperature of 850 °C, an area specific resistance of only 0.070 $\Omega\,cm^2$ at 550 °C was achieved for a modified BSCF cathode. The reaction mechanism for oxygen reduction over the silver-modified BSCF cathodes was proposed:

(a) Diffusion of O_2 (gas) in gas phase through the porous layer; (1)
(b) Dissociative adsorption of O_2 to form O_{ad} on the silver-modified BSCF cathode:
  (2) $O_2\,(gas) \rightarrow 2O_{ad}\,(BSCF)$
  (2′) $O_2\,(gas) \rightarrow 2O_{ad}\,(Ag)$
  (2″) $O_2\,(gas) \rightarrow 2O_{ad}\,(BSCF/Ag)$
(c) Surface diffusion of O_{ad} to the effective reaction zone (ERZ):
  (3) $O_{ad}\,(BSCF) \rightarrow O_{ad}\,(ERZ)$
  (3′) $O_{ad}\,(Ag) \rightarrow O_{ad}\,(ERZ)$
  (3″) $O_{ad}\,(BSCF/Ag) \rightarrow O_{ad}\,(ERZ)$
(d) Charge transfer at ERZ:
  (4) $O_{ad}\,(ERZ) + V_O^{\bullet\bullet}\,(BSCF) + 2e^- \rightarrow O^{2-}\,(BSCF)$
(e) Ionic transfer of O^{2-} from BSCF into SDC:
  (5) $O^{2-}\,(BSCF) \rightarrow O^{2-}\,(SDC)$

where O_{ad} stands for the adsorbed oxygen atom and $V_O^{\bullet\bullet}$ is the oxygen vacancies in BSCF. Since the porosity is sufficiently high, the activation polarization resistance of step 1 can be reasonably ignored. ORR processes over the silver-modified BSCF cathode are schematically shown in Fig. 6. For the pure BSCF cathode, the oxygen exchange was controlled by the adsorption of O_2 (step 2) and surface diffusion of O_{ad} (step 3). By using silver as a promoter, the adsorption of O_2 is improved because the effective zone for O_2 adsorption is extended from the pure BSCF surface (step 2) to Ag particles (step 2′) or the BSCF/Ag boundary (step 2″). The optimal activation energy for the diffusion process (including steps 2 and 3) of BSCF-3Ag is only 86 kJ mol^{-1}, while it increased to 112 kJ mol^{-1} as the Ag loading increased to 30 wt%. Meanwhile, the oxygen surface diffusion resistance (R_{E2}) of BSCF-3Ag is the lowest compared to those of BSCF-0.3Ag and BSCF-30Ag. This suggests that the surface diffusion of O_{ad} on Ag particles (step 3′) may be slower than on pure BSCF (step 3), so the excessive Ag loading allows for the diffusion process to be controlled by the surface diffusion. For the enhancement of electrical conductivity by Ag, oxygen chemical reduction reaction involving a charge transfer process (step 4) can also be dramatically improved. On the other hand, some of the surface oxygen vacancies could also be covered by the Ag particles, which would reduce active sites for ORR. Therefore, the initial improvement in the electrochemical performance with Ag incorporation (up to ~3.0 wt%) is due to the increase in the electronic conductivity and catalytic activity, while adequate numbers of reaction sites are maintained. However, when the silver content reached 30 wt% of BSCF, a considerable number of the reaction sites for the oxygen reduction process were occupied by the Ag particles, which blocked the oxide ion conduction [194], consequently resulting in a decrease of electrochemical performance. Due to the excellent performance of Ag, the improved electrochemical performance was also obtained by using BSCF-GDC-Ag or BSCF-SDC/BSCF-SDC-Ag double layers as the cathode [195,196].

The current collector on the top of the cathode also dramatically influences the electrochemical performance. Jiang et al. investigated the effect of contact area between the electrode and current collector (i.e., the interconnect) on the performance of anode-supported SOFCs using a current collector with various contact areas on the (Pr,Sr)MnO_3 (PSM) cathode side [197]. The cell resistance decreased significantly with increasing contact area between the PSM cathode and the current collector . The cell resistance decreased from 1.43 to 0.19 $\Omega\,cm^2$ at 800 °C by increasing the contact area from 4.6 to 27.2%. The results indicated that the contact area of the current collector may affect the cell performance. This shows that the constriction effect fre-

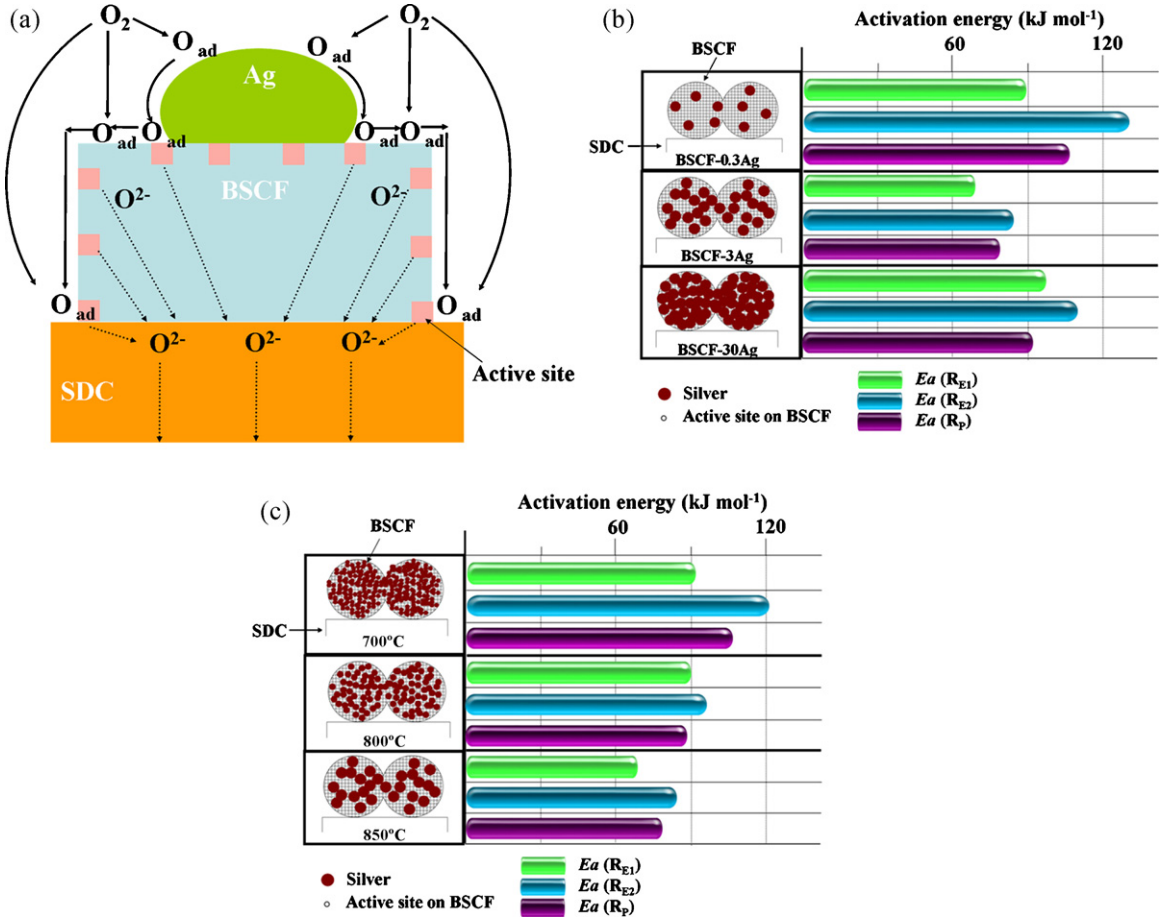

Fig. 6. Schematic of ORR processes on silver-modified BSCF cathode (a) [193]. Effect of Ag loading (b) and firing temperature (c) on the electrocatalytic activity of Ag-modified BSCF cathodes.

quently observed in solid electrolyte cells occurs not only at the electrode/electrolyte interface but also at the interface of the electrode/current collector. The current collection may have an even more pronounced effect on the BSCF cathode due to its lower electronic conductivity. The results of the ASRs of the BSCF cathodes reported by different groups greatly varied from each other despite similar operating conditions. Except for the differences from the powder synthesis and cathode preparation, the current collector could also be contributing to the distinction. Zhou et al. studied the effect of contact between the BSCF cathode and current collector on the performance of SOFCs. The $LaCoO_3$/Ag double layers improved cathode performance dramatically over that with the current collector [198].

6.2. Thermal expansion behavior

TECs of both the electrolyte and electrode layers should be well matched to ensure long-term operational stability of the SOFCs. One distinguishing feature of cobalt-based cathode materials, including BSCF, is their high TECs. The TEC of BSCF is much larger than most of the electrolytes [199]. Due to this mismatch, in some cases, the high TEC even resulted in the BSCF cathode's peeling off from the GDC/ScSZ electrolyte [127]. The chemical and thermal expansion of BSCF between 873 and 1173 K and oxygen partial pressures of 1×10^{-3} to 1 atm were determined by in situ neutron diffraction by McIntosh et al. [163]. In the range covered by the experiments, the thermal and chemical expansion coefficients are 19.0(5)–20.8(6) $\times 10^{-6}\,K^{-1}$ and 0.016(2)–0.026(4), respectively. The thermal expansion was attributed to crystal expansion from harmonic atomic vibrations, which depend on the electrostatic attraction forces within the lattice [200], while the chemical expansion was induced by both the cobalt ion spin transition and the thermal/chemical reduction of cobalt ions to lower oxidation states [201].

Zhou et al. reported that the TEC of BSCF could be reduced by introducing A-site cation deficiency into BSCF, i.e. $(Ba_{0.5}Sr_{0.5})_{1-x}Co_{0.8}Fe_{0.2}O_{3-\delta}$ ($(BS)_{1-x}CF$) oxides [202]. They found that the TEC was highly dependent upon both the A-site cation deficiency fraction (x) and the selected temperature range. The TECs decreased with increasing A-site cation deficiency, especially in the 450–750 °C temperature range. Both Kostogloudis and Ftikos, and Hansen and Vels Hansen reported similar trends for $(La_{0.6}Sr_{0.4})_{1-x}Co_{0.2}Fe_{0.8}O_{3-\delta}$ ($x = 0.00$–0.15) oxides [183,184]. Increased electrostatic attraction resulting from the decrease of the lattice parameter may be responsible for this phenomenon. The TEC of the $(BS)_{1-x}CF$ perovskites was also closely correlated with the chemical expansion effects resulting from changes in the point defect concentration and the spin state of cobalt ions [202]. Ge et al. also found that the A-site deficient BSCF also had higher oxygen permeability due to the improved oxygen ionic conductivity [203]. However, the increase in A-site cation deficiency resulted in a steady increase in cathode polarization resistance because of formation of impurities at the cathode/electrolyte interface and reduced electronic conductivity. A single SOFC equipped with a $BS_{0.97}CF$ cathode exhibited peak power densities of 694 and 893 mW cm^{-2} at 600 and 650 °C, respectively, and these results were comparable with those obtained with a BSCF cathode. Considering the fact that low TEC may improve long-term stability of

the electrode, slightly A-site cation-deficient $(BS)_{1-x}CF$ oxides were still highly promising cathodes for IT-SOFCs.

6.3. A- or B-site doping of BSCF

Li et al. reported that by doping a rare earth metal into A-sites of BSCF with the formation of $(Ba_{0.5}Sr_{0.5})_{1-x}Sm_xCo_{0.8}Fe_{0.2}O_{3-\delta}$ (BSSCF; $x = 0.05$–0.15), the conductivity was improved, e.g., about 21.2% improvement as compared to pristine BSCF at 500 °C for the $x = 0.15$ compound [204,205]. Electrochemical impedance spectra at intermediate temperatures also revealed a better electrochemical performance of BSSCF than BSCF; e.g., the total resistance values of BSSCF electrode is nearly 50% lower than that of BSCF. However, the TEC of these doped compounds is 19.1–20.3 × 10^{-6} K^{-1} from 30 to 800 °C, which is even higher than the values of BSCF. The doping of La or Nd had a similar effect on the cathode performance [206,207].

Serra et al. studied several elements as potential A-site substituents in the perovskite $A_{0.68}Sr_{0.3}Fe_{0.8}Co_{0.2}O_{3-\delta}$ system [172], including La, Pr, Sm, Nd, Er, Eu, Gd, Dy, and Ba. With respect to the electrochemical behavior when operating as an SOFC cathode, two different situations have been found depending on the operating temperature. At high temperatures (850–900 °C), La- and Pr-based materials are by far the best performing materials, achieving values of 1.4 and 1.25 A cm^{-2}, respectively, at 0.8 V and 900 °C. However, at lower temperatures (650 °C), other materials, based on Ba and Sm, appear to perform at least similarly to the Pr-based cathode. Indeed, Ba- and Sm-based cathodes show the lowest activation energies. This fact is interpreted as a result of the catalytic activity of the surface species involved in oxygen reduction and incorporation into the perovskite lattice. On the other hand, it was found that Pd incorporation into the Pr-based cathode resulted in strong reduction of the area-specific resistance.

The substitution of cobalt ion by more chemically stable ions, such as Ti, is expected to decrease the TEC of the compounds and improve the chemical stability with CeO_2-based materials [208]. $Ba_{0.6}Sr_{0.4}Co_{1-y}Ti_yO_{3-\delta}$ (BSCT) oxides showed a TEC of about 14 × 10^{-6} K^{-1} at $y = 0.2$, which results in a good physical compatibility of BSCT with GDC electrolyte. BSCT also shows excellent thermal cyclic stability of electrical conductivity and good chemical stability with GDC. These properties make BSCT a promising cathode candidate for intermediate temperature solid-oxide fuel cells (IT-SOFCs).

Ovenstone et al. used in situ X-ray diffraction to investigate the phase stability of $Ba_{0.5}Sr_{0.5}Co_yFe_{1-y}O_{3-\delta}$ ($y = 0$–1) [209]. The thermal decomposition processes both in low partial pressures of oxygen (0.21 to 10^{-5} atm P_{O_2}) and in reducing conditions have been studied in detail. BSCF manifested excellent stability down to 10^{-5} atm P_{O_2}; however, it decomposed through a complex series of oxides under more reducing conditions. Increasing the cobalt content resulted in a decrease in the temperature range of stability of the material under 4% H_2 in N_2, with the initial decomposition taking place at 375, 425, 550, 600, 650, and 675 °C, for $y = 1$, 0.8, 0.6, 0.4, 0.2, and 0, respectively. Wang et al. reported that by replacing Co with Zn, developing $Ba_{0.5}Sr_{0.5}Zn_{0.2}Fe_{0.8}O_{3-\delta}$ (BSZF) perovskite oxide, the corresponding membrane fabricated from BSZF exhibited higher oxygen permeation flux (1.45 mm in thickness, 0.35 ml min^{-1} cm^{-2}) [210]. Furthermore, it showed good chemical stability even under a low oxygen partial pressure of 10^{-12} atm, which is also preferred for SOFC cathodes. Wei et al. synthesized and examined BSZF as a new cobalt-free cathode for IT-SOFCs [211]. The electrical conductivity was relatively low, with a maximum value of 9.4 S cm^{-1} at about 590 °C, mainly caused by the high concentration of oxygen vacancy and the doping of bivalent zinc in B-sites. At 650 °C and under open circuit condition, symmetrical BSZF cathode on an SDC electrolyte showed polarization resistances (R_p) of 0.48 and 0.35 Ω cm^2 in air and oxygen, respectively. The dependence of R_p on oxygen partial pressure indicated that the rate-limiting step for oxygen reduction was oxygen adsorption/desorption kinetics. Using BSZF as the cathode, the wet hydrogen fueled Ni/SDC anode-supported single cell exhibited peak power densities of 392 and 626 mW cm^{-2} at 650 °C when stationary air and oxygen flux were used as oxidants, respectively.

7. New issues raised by BSCF

The instability of the perovskite oxides containing alkaline-earth elements in the presence of CO_2 and H_2O emerges as one of the limiting factors for the practical application in reduced temperature SOFCs, since the ambient air typically contains a minor amount of CO_2. Arnold et al. [212] published results concerning the influence of CO_2 on the oxygen permeation performance and the microstructure of perovskite-type BSCF oxides. They found that pure CO_2 as the sweep gas at 875 °C caused an immediate stop of the oxygen permeation flux, which, however, could be recovered by sweeping with pure helium. Examination of the microstructure clearly indicated the decomposition of the perovskite structure up to a depth of 40–50 μm when it was exposed to CO_2 for more than 4300 min.

Some studies proved that the presence of carbonates is very detrimental to electrocatalysis by the BSCF cathode. Zhou et al. found that when the Ag/BSCF composite cathodes were prepared by electroless deposition using N_2H_4 and HCHO as reducing agents, the results were very different [213]. As compared to a pristine BSCF electrode, the electrochemical performance of the composite cathode was improved by using N_2H_4 as the reducing agent. The ASR of N_2H_4-reduced Ag/BSCF was as low as 0.038 Ω cm^2 at 600 °C. However, when the HCHO was used as the reducing agent, the carbonates in the family of $Ba_xSr_{1-x}CO_3$ were formed during the preparation, which blocked the active sites for oxygen adsorption and reduction reactions and led to an increase in the polarization resistances of both the charge-transfer process and the diffusion process. Bucher et al. suggested that oxygen exchange at 300–700 °C can be significantly impaired by CO_2-containing atmospheres [214]. Therefore, reducing agents that could lead to the formation of carbonates are not recommended in the preparation of silver-modified perovskite electrodes that contain Ba and/or Sr alkaline-earth metal ions.

The effect of CO_2 on the performance of BSCF cathode was systematically studied by Yan et al. [215–218]. They pointed out that the BSCF cathode was susceptible to CO_2 attack at 450–750 °C. A decrease of the cell performance and increase of the polarization resistance were observed when CO_2 was supplied to the cathode gas line [215]. A detailed surface analysis of the BSCF cathode after exposure to 1% CO_2/O_2 at 450 °C for 24 h revealed that the cathode surface was destroyed and the carbonates of Sr and Ba were formed on the top of the cathode layer [216]. The adsorption of CO_2 on BSCF perovskite oxides in the absence and presence of O_2 and H_2O at various temperatures was investigated by temperature programmed desorption (TPD). XRD was used to characterize the phase of the samples before and after adsorption. No CO_2 desorption peak was observed when CO_2 was adsorbed on BSCF at room temperature. A CO_2 desorption peak from the decomposition of surface $Ba_{0.4}Sr_{0.6}CO_3$ appeared after CO_2 was adsorbed at 400–700 °C. The reactivity of CO_2 with BSCF increased with increasing temperature, and the resulting carbonates became more stable. When CO_2 and O_2 were co-adsorbed, the CO_2 desorption peak shifted to a lower temperature, and the peak area decreased compared to when pure CO_2 was adsorbed, which was due to the competitive adsorption of CO_2 and O_2. The adsorption of CO_2 on BSCF was promoted in the presence of H_2O. A CO_2 desorption peak ranging from ~250 to 500 °C, assigned to the decomposition of the bicarbonate, was observed when H_2O was added. It was proposed that the presence of both H_2O and CO_2 could inhibit the adsorption of O_2, resulting

in the increase of oxygen vacancies and a more serious poisoning effect. It was found that the desorption area decreased following the order: $CO_2 > CO_2–O_2–H_2O > CO_2–O_2$. This result confirmed that H_2O can aggravate the poisoning effect of CO_2, while the presence of O_2 helped to stabilize the perovskite structure. The amount of CO_2 adsorbed on BSCF increased when the barium doping level increased from 0.3 to 1, which should be ascribed to the higher thermodynamic stability of $BaCO_3$ compared to $SrCO_3$ [218].

The structural instability of cubic BSCF phase at low temperature in air is another particular issue of concern. Švarcová et al. reported that the cubic BSCF becomes unstable in air at intermediate temperatures and gradually transforms to a hexagonal perovskite on cooling, which may cause the questions regarding the long-term stability of such a highly defective material under the operating conditions of an IT-SOFC [219]. Fortunately, they showed that the transformation of the cubic to hexagonal polymorph of BSCF can be rationalized by the Goldschmidt tolerance factor and accordingly suppressed by appropriate substitutions.

8. Summary and outlook

In summary, BSCF is a very promising cathode for IT-SOFCs due to its excellent electrocatalytic activity for oxygen reduction at temperatures below 650 °C. The high electrochemical performance of BSCF is ascribed to its high oxygen vacancy concentration, which increases not only the oxygen bulk diffusion rate but also the surface exchange kinetics. To further promote the electrocatalytic activity of BSCF, the relatively slow oxygen surface processes should be optimized by introducing additional oxygen vacancies or by modification with electronic conducting materials, such as $LaCoO_3$ and Ag. The high thermal expansion coefficient of BSCF can be modestly reduced by using A-site deficient BSCF, which is beneficial for the long-term stability of the cell.

Severe degradation of the surface oxygen exchange coefficient is observed for the BSCF cathode exposed to a CO_2-containing atmosphere. Accordingly, extremely pure air feed is required as the oxidant at the cathode when employing BSCF as the cathode at low operating temperatures, which would increase the operation cost of the fuel cell. Such an open question constitutes challenging and essential topics for future investigations.

Acknowledgements

This work was supported by the National Natural Science Foundation of China under contract Nos. 20703024, and 20676061, by the National 863 program under contract No. 2007AA05Z133, and by the National Basic Research Program of China under contract No. 2007CB209704.

References

[1] N.Q. Minh, J. Am. Ceram. Soc. 76 (1993) 563.
[2] S.C. Singhal, Solid State Ionics 135 (2000) 305.
[3] O. Yamamoto, Electrochim. Acta 45 (2000) 2423.
[4] B.C.H. Steele, A. Heinzel, Nature 414 (2001) 345.
[5] S.M. Haile, Acta Mater. 51 (2003) 5981.
[6] W. Nernst, Z. Elektrochem. 6 (1899) 41.
[7] W. Nernst, DRP 104872 (1897).
[8] W. Nernst, US Patent 685,730 (1899).
[9] S. McIntosh, R.J. Gorte, Chem. Rev. 104 (2004) 4845.
[10] S.P.S. Badwal, K. Foger, Ceram. Int. 22 (1996) 257.
[11] S.C. Singhal, K. Kendall, High Temperature Solid Oxide Fuel Cells: Fundamentals, Design and Applications, Elsevier Advanced Technology, UK, 2003.
[12] W. Zhou, H.G. Shi, R. Ran, R. Cai, Z.P. Shao, W.Q. Jin, J. Power Sources 184 (2008) 229.
[13] H.X. Gu, R. Ran, W. Zhou, Z.P. Shao, J. Power Sources 172 (2007) 704–712.
[14] B. Lin, W. Sun, K. Xie, Y. Dong, D. Dong, X. Liu, J. Gao, G. Meng, J. Alloys Compd. 465 (2008) 285–290.
[15] T. Yamaguchi, S. Shimizu, T. Suzuki, Y. Fujishiro, M. Awano, Electrochem. Commun. 10 (2008) 1381–1383.
[16] M.G. Bellino, D.G. Lamas, N.E. Walsöe de Reca, Adv. Funct. Mater. 16 (2006) 107.
[17] A. Infortuna, A.S. Harvey, L.J. Gauckler, Adv. Funct. Mater. 18 (2008) 127.
[18] J.H. Shim, C.-C. Chao, H. Huang, F.B. Prinz, Chem. Mater. 19 (2007) 3850.
[19] K. Mehta, R. Xu, Y.V. Virkar, J. Sol–Gel Sci. Technol. 11 (1998) 203.
[20] W.T. Bao, W. Zhu, G.Y. Zhu, J.F. Gao, G.Y. Meng, Solid State Ionics 176 (2005) 669.
[21] J. Liu, S.A. Barnett, J. Am. Ceram. Soc. 85 (2002) 3096.
[22] Z. Cai, T.N. Lan, S. Wang, M. Dokiya, Solid State Ionics 152–153 (2002) 583.
[23] W.T. Bao, Q.B. Chang, R.Q. Yan, G.Y. Meng, J. Membr. Sci. 252 (2005) 175.
[24] J. Will, A. Mitterdorfer, C. Kleinlogel, D. Perednis, L.J. Gauckler, Solid State Ionics 131 (2000) 79.
[25] D. Beckel, A. Bieberle-Hütter, A. Harvey, A. Infortuna, U.P. Muecke, M. Prestat, J.L.M. Rupp, L.J. Gauckler, J. Power Sources 173 (2007) 325.
[26] S.P.S. Badwal, F.T. Ciacchi, D. Milosevic, Solid State Ionics 136–137 (2000) 91.
[27] M. Mori, T. Abe, H. Itoh, O. Yamamoto, Y. Takeda, T. Kawahara, Solid State Ionics 74 (1994) 157.
[28] V.V. Kharton, F.M. Figueiredo, L. Navarro, E.N. Naumovich, A.V. Kovalevsky, A.A. Yaremchenko, A.P. Viskup, A. Carneiro, F.M.B. Marques, J.R. Frade, J. Mater. Sci. 36 (2001) 1105.
[29] J.W. Stevenson, K. Hasinska, N.L. Canfield, T.R. Armstrong, J. Electrochem. Soc. 147 (2000) 3213.
[30] A.A. Yaremchenko, V.V. Kharton, E.N. Naumovich, F.M.B. Marques, J. Electroceram. 4 (1999) 233.
[31] S.A. Kramer, H.L. Tuller, Solid State Ionics 82 (1995) 15.
[32] H. Arikawa, H. Nishiguchi, T. Ishihara, Y. Takita, Solid State Ionics 136–137 (2000) 31.
[33] A.A. Yaremchenko, M. Avdeev, V.V. Kharton, A.V. Kovalevsky, E.N. Naumovich, F.M.B. Marques, Mater. Chem. Phys. 77 (2002) 552.
[34] V.V. Kharton, F.M.B. Marquesa, A. Atkinson, Solid State Ionics 174 (2004) 135.
[35] T. Ishihara, H. Matsuda, Y. Takita, J. Am. Chem. Soc. 116 (1994) 3801.
[36] M. Feng, J.B. Goodenough, Eur. J. Solid State Inorg. Chem. 31 (1994) 663.
[37] K. Zheng, B.C.H. Steele, M. Sahibzada, I.S. Metcalfe, Solid State Ionics 86–88 (1996) 1241.
[38] M. Sahibzada, B.C.H. Steele, K. Zheng, R.A. Rudkin, I.S. Metcalfe, Catal. Today 38 (1997) 459.
[39] B.C.H. Steele, Solid State Ionics 129 (2000) 95.
[40] Y. Zheng, R. Ran, H.X. Gu, R. Cai, Z.P. Shao, J. Power Sources 185 (2008) 641–648.
[41] Y. Zheng, C.M. Zhang, R. Ran, R. Cai, Z.P. Shao, D. Farrusseng, Acta Mater. 57 (2009) 1165–1175.
[42] Y. Zheng, R. Ran, Z.P. Shao, J. Phys. Chem. C 112 (2008) 18690–18700.
[43] S.P. Jiang, J. Mater. Sci. 43 (2008) 6799.
[44] E.P. Murray, T. Tsai, S.A. Barnett, Solid State Ionics 110 (1998) 235.
[45] E.P. Murray, S.A. Barnett, Solid State Ionics 143 (2001) 265.
[46] M.J. Jorgensen, S. Primdahl, M. Mogensen, Electrochim. Acta 44 (1999) 4195.
[47] M.J.L. Ostergard, C. Clausen, C. Bagger, M. Mogensen, Electrochim. Acta 40 (1995) 1971.
[48] Z. Lei, Q. Zhu, L. Zhao, J. Power Sources 161 (2006) 1169.
[49] S.P. Jiang, W. Wang, J. Electrochem. Soc. 152 (2005) A1398.
[50] W. Zhou, Z.P. Shao, R. Ran, H.X. Gu, W.Q. Jin, N.P. Xu, J. Am. Ceram. Soc. 91 (2008) 1155.
[51] W. Zhou, Z.P. Shao, R. Ran, W.Q. Jin, N.P. Xu, Chem. Commun. (2008) 5791.
[52] W. Zhou, Z.P. Shao, R. Ran, R. Cai, Electrochem. Commun. 10 (2008) 1647.
[53] M.T. Colomer, B.C.H. Steele, J.A. Kilner, Solid State Ionics 147 (2002) 41–48.
[54] J.-M. Bae, B.C.H. Steele, Solid State Ionics 106 (1998) 247–253.
[55] B.C.H. Steele, J.-M. Bae, Solid State Ionics 106 (1998) 255–261.
[56] D. Waller, J.A. Lane, J.A. Kilner, B.C.H. Steele, Mater. Lett. 27 (1996) 225–228.
[57] D. Waller, J.A. Lane, J.A. Kilner, B.C.H. Steele, Solid State Ionics 86–88 (1996) 767–772.
[58] T. Kawada, K. Masuda, J. Suzuki, A. Kaimai, K. Kawamura, Y. Nigara, J. Mizusaki, H. Yugami, H. Arashi, N. Sakai, H. Yokokawa, Solid State Ionics 121 (1999) 271–279.
[59] M. Sase, D. Ueno, K. Yashiro, A. Kaimai, T. Kawada, J. Mizusaki, J. Phys. Chem. Solids 66 (2005) 343–348.
[60] H.J.M. Bouwmeester, M.W. Den Otter, B.A. Boukamp, J. Solid State Electrochem. 8 (2004) 599–605.
[61] R.A. De Souza, J.A. Kilner, Solid State Ionics 126 (1999) 153–161.
[62] R.A. De Souza, J.A. Kilner, Solid State Ionics 106 (1998) 175–187.
[63] T. Hibino, A. Hashimoto, T. Inoue, J. Tokuno, S. Yoshida, M. Sano, Science 288 (2000) 2031.
[64] C.R. Xia, F.L. Chen, M.L. Liu, Electrochem. Solid-State Lett. 4 (2001) A52.
[65] C.R. Xia, M.L. Liu, Solid State Ionics 144 (2001) 249.
[66] V. Dusastre, J.A. Kilner, Solid State Ionics 126 (1999) 163.
[67] J. Fleig, Annu. Rev. Mater. Res. 33 (2003) 361.
[68] S.B. Adler, Chem. Rev. 104 (2004) 4791.
[69] Z.P. Shao, S.M. Haile, Nature 431 (2004) 170.
[70] Z.P. Shao, S.M. Haile, J. Ahn, P.D. Ronney, Z.L. Zhan, S.A. Barnett, Nature 435 (2005) 795.
[71] Z.P. Shao, W.S. Yang, Y. Cong, H. Dong, J.H. Tong, G.X. Xiong, J. Membr. Sci. 172 (2000) 177.
[72] Z.P. Shao, G.X. Xiong, J.H. Tong, H. Dong, W.S. Yang, Sep. Purif. Tech. 25 (2001) 419.
[73] Z.P. Shao, G.X. Xiong, H. Dong, W.S. Yang, L.W. Lin, Sep. Purif. Tech. 25 (2001) 97.

[74] Z.P. Shao, H. Dong, G.X. Xiong, Y. Cong, W.S. Yang, J. Membr. Sci. 183 (2001) 181.
[75] H.H. Wang, Y. Cong, W.S. Yang, Chem. Commun. (2002) 1468.
[76] H. Lu, J.H. Tong, Y. Cong, W.S. Yang, Catal. Today 104 (2005) 154.
[77] H.H. Wang, Y. Cong, W.S. Yang, Catal. Today 82 (2003) 157.
[78] C.-S. Chen, S.-J. Feng, S. Ran, D.-C. Zhu, W. Liu, H.J.M. Bouwmeester, Angew. Chem. Int. Ed. 42 (2003) 5196.
[79] W. Zhu, W. Han, G. Xiong, W. Yang, Catal. Today 104 (2005) 149.
[80] C.-L. Chang, T.-C. Lee, T.-J. Huang, J. Solid State Electrochem. 2 (1998) 291–298.
[81] Q. Li, H. Zhao, L. Huo, L. Sun, X. Cheng, J.-C. Grenier, Electrochem. Commun. 9 (2007) 1508–1512.
[82] M.J. Escudero, A. Aguadero, J.A. Alonso, L. Daza, J. Electroanal. Chem. 611 (2007) 107–116.
[83] F. Zhao, X. Wang, Z. Wang, R. Peng, C. Xia, Solid State Ionics 179 (2008) 1450–1453.
[84] J.-M. Bae, B.C.H. Steele, J. Electroceram. 3 (1999) 37–46.
[85] T. Hibino, A. Hashimoto, M. Suzuki, M. Sano, J. Electrochem. Soc. 149 (2002) A1503–A1508.
[86] K. Zhang, L. Ge, R. Ran, Z.P. Shao, S.M. Liu, Acta Mater. 56 (2008) 4876–4889.
[87] D.J. Chen, R. Ran, K. Zhang, J. Wang, Z.P. Shao, J. Power Sources 188 (2009) 96–105.
[88] A. Tarancon, S.J. Skinner, R.J. Chater, F. Hernandez-Ramirez, J.A. Kilner, J. Mater. Chem. 17 (2007) 3175–3181.
[89] G. Kim, S. Wang, A.J. Jacobson, L. Reimus, P. Brodersen, C.A. Mims, J. Mater. Chem. 17 (2007) 2500–2505.
[90] J.E.H. Sansom, E. Kendrick, H.A. Rudge-Pickard, M.S. Islam, A.J. Wright, P.R. Slater, J. Mater. Chem. 15 (2005) 2321–2327.
[91] K.T. Lee, A. Manthiram, Chem. Mater. 18 (2006) 1621–1626.
[92] M.A. Peña, J.L.G. Fierro, Chem. Rev. 101 (2001) 1981.
[93] V.M. Goldschmidt, Skr. Nor. Videnk-Akad., Kl. 1: Mat.-Naturvidensk. Kl. No. 8 (1926).
[94] C.P. Khattak, F.F.Y. Wang, in: K.A. Gschneider Jr., L. Eyring (Eds.), Handbook of the Physics and Chemistry of Rare Earths, North-Holland Publisher, Amsterdam, 1979, p. 525.
[95] J.B. Goodenough, J.M. Longo, In: K.H. Hellwege, A.M. Helwege (Eds.), Landolt-Bronstein New Series, vol. 4, part A, Springer-Verlag, Berlin, 1970, p. 126.
[96] J.B. Goodenough, in: C.N.R. Rao (Ed.), Solid State Chemistry, Marcel Dekker, New York, 1974, p. 215.
[97] H. Koster, F.H.B. Mertins, Powder Diffract. 18 (2003) 56–59.
[98] Z.Q. Deng, W.S. Yang, W. Liu, C.S. Chen, J. Solid State Chem. 179 (2006) 362.
[99] J. Rodriguez, J.M. Gonzalez-Calbet, J.C. Grenier, J. Pannetier, M. Anne, Solid State Commun. 62 (1987) 231.
[100] J. Rodriguez, J.M. Gonzalez-Calbet, Mater. Res. Bull. 21 (1986) 429.
[101] J.C. Grenier, L. Fournes, M. Pouchard, P. Hagenmuller, Mater. Res. Bull. 21 (1986) 441.
[102] Y. Ito, R.F. Klie, N.D. Browning, T.J. Mazanec, J. Am. Ceram. Soc. 85 (2002) 969.
[103] V.V. Vashook, M.V. Zinkevich, H. Ullmann, J. Paulsen, N. Trofimenko, K. Teske, Solid State Ionics 99 (1997) 23.
[104] S. Ikeda, O. Sakurai, K. Uematsu, N. Mizutani, M. Kato, J. Mater. Sci. 20 (1985) 4593.
[105] C.H. Chen, H.J.M. Bouwmeester, R.H.E. van Doorn, H. Kruidhof, A.J. Burggraaf, Solid State Ionics 98 (1997) 7.
[106] K. Zhang, R. Ran, L. Ge, Z.P. Shao, W.Q. Jin, N.P. Xu, J. Membr. Sci. 323 (2008) 436.
[107] P.Y. Zeng, R. Ran, Z.H. Chen, W. Zhou, H.X. Gu, Z.P. Shao, S.M. Liu, J. Alloys Compd. 455 (2008) 465.
[108] Y. Teraoka, H.M. Zhang, S. Furukawa, N. Yamazoe, Chem. Lett. 14 (1985) 1743.
[109] Y. Teraoka, T. Nobunaga, N. Yamazoe, Chem. Lett. 17 (1988) 503.
[110] Y. Teraoka, T. Nobunaga, K. Okamoto, N. Miura, N. Yamazoe, Solid State Ionics 48 (1991) 207.
[111] L. Qiu, T.H. Lee, L.M. Liu, Y.L. Yang, A.J. Jacobson, Solid State Ionics 76 (1995) 321.
[112] S. Pei, M.S. Kleefisch, T.P. Kobylinski, J. Faber, C.A. Udovich, V. Zhang-McCoy, B. Dabrowski, U. Balachandran, R.L. Mieville, R.B. Poeppel, Catal. Lett. 30 (1995) 201.
[113] H. Kruidhof, H.J.M. Bouwmeester, R.H.E. van Doorn, A.J. Burggraaf, Solid State Ionics 63–65 (1993) 816.
[114] V.V. Kharton, V.N. Tikhonovich, S.B. Li, E.N. Naumovich, A.V. Kovalevsky, A.P. Viskup, I.A. Bashmakav, A.A. Yaremchenko, J. Electrochem. Soc. 145 (1998) 1363.
[115] H. Yokokawa, N. Sakai, T. Kawada, M. Dokiya, Solid State Ionics 52 (1992) 43.
[116] S. McIntosh, J.F. Vente, W.G. Haije, D.H.A. Blank, H.J.M. Bouwmeester, Solid State Ionics 177 (2006) 1737.
[117] B. Wei, Z. Lü, X. Huang, J. Miao, X. Sha, X. Xin, W. Su, J. Eur. Ceram. Soc. 26 (2006) 2827.
[118] Z.H. Chen, R. Ran, W. Zhou, Z.P. Shao, S.M. Liu, Electrochim. Acta 52 (2007) 7343.
[119] C.A.J. Fisher, M. Yoshiya, Y. Iwamoto, J. Ishii, M. Asanuma, K. Yabuta, Solid State Ionics 177 (2007) 3425.
[120] Q.L. Liu, K.A. Khor, S.H. Chan, J. Power Sources 161 (2006) 123.
[121] K. Wang, R. Ran, W. Zhou, H.X. Gu, Z.P. Shao, J. Ahn, J. Power Sources 179 (2008) 60.
[122] J. Peña-Martínez, D. Marrero-López, J.C. Ruiz-Morales, B.E. Buergler, P. Núñez, L.J. Gauckler, Solid State Ionics 177 (2006) 2143.
[123] Y. Lin, R. Ran, Y. Zheng, Z.P. Shao, W.Q. Jin, N.P. Xu, J. Ahn, J. Power Sources 180 (2008) 15.
[124] R.R. Peng, Y. Wu, L.Z. Yang, Z.Q. Mao, Solid State Ionics 177 (2006) 389.
[125] Q. Zhu, T. Jin, Y. Wang, Solid State Ionics 177 (2006) 1199.
[126] Z. Duan, M. Yang, A. Yan, Z. Hou, Y. Dong, Y. Chong, M. Cheng, W. Yang, J. Power Sources 160 (2006) 57.
[127] Y.H. Lim, J. Lee, J.S. Yoon, C.E. Kim, H.J. Hwang, J. Power Sources 171 (2007) 79.
[128] L. Wang, R. Merkle, F.S. Baumann, ECS Trans. 7 (2007) 1015–1024.
[129] M. Gaudon, C. Laberty-Robert, F. Ansart, L. Dessemond, P. Stevens, J. Power Sources 133 (2004) 214.
[130] K.T. Lee, A. Manthiram, J. Power Sources 158 (2006) 1202.
[131] N.P. Bansal, Z.M. Zhong, J. Power Sources 158 (2006) 148.
[132] W. Zhou, Z.P. Shao, R. Ran, W.Q. Jin, N.P. Xu, Mater. Res. Bull. 43 (2008) 2248.
[133] L. Ge, W. Zhou, R. Ran, Z.P. Shao, S.M. Liu, J. Alloys Compd. 450 (2008) 338.
[134] R.J. Bell, G.J. Millar, J. Drennan, Solid State Ionics 131 (2000) 211.
[135] S. Royer, F. Bérubé, S. Kaliaguine, Appl. Catal. A 282 (2005) 273.
[136] X. Zhu, Y. Cong, W. Yang, J. Membr. Sci. 283 (2006) 158.
[137] J. Sfeir, S. Vaucher, P. Holtappels, U. Vogt, H.-J. Schindler, J. Van Herle, E. Suvorova, P. Buffat, D. Perret, N. Xanthopoulos, O. Bucheli, J. Eur. Ceram. Soc. 25 (2005) 1991.
[138] L. Tan, X. Gu, L. Yang, W. Jin, L. Zhang, N. Xu, J. Membr. Sci. 212 (2003) 157.
[139] W. Zhou, Z.P. Shao, W.Q. Jin, J. Alloys Compd. 426 (2006) 368.
[140] S. Lee, Y. Lim, E.A. Lee, H.J. Hwang, J.-W. Moon, J. Power Sources 157 (2006) 848.
[141] B. Liu, Y. Zhang, J. Alloys Compd. 453 (2008) 418.
[142] A. Subramania, T. Saradha, S. Muzhumathi, J. Power Sources 165 (2007) 728.
[143] W. Zhou, R. Ran, Z.P. Shao, H.X. Gu, W.Q. Jin, N.P. Xu, J. Power Sources 174 (2007) 237.
[144] W. Zhou, Z.P. Shao, W.Q. Jin, Chin. Chem. Lett. 17 (2006) 1353.
[145] J. Martynczuk, M. Arnold, H. Wang, J. Caro, A. Feldhoff, Adv. Mater. 19 (2007) 2134.
[146] N.Q. Minh, T. Takahashi, Science and Technology of Ceramic Fuel Cell, Elsevier, NY, 1995.
[147] A.S. Joshi, K.N. Grew, A.A. Peracchio, W.K.S. Chiu, J. Power Sources 164 (2007) 631.
[148] R.M.C. Clemmer, S.F. Corbin, Solid State Ionics 166 (2004) 251.
[149] M. Mamak, N. Coombs, G. Ozin, J. Am. Chem. Soc. 122 (2000) 8932.
[150] E.O. Chi, Y.N. Kim, J.C. Kim, N.H. Hur, Chem. Mater. 15 (2003) 1929.
[151] M. Sadakane, T. Asanuma, J. Kubo, W. Ueda, Chem. Mater. 17 (2005) 3546.
[152] J.C. Ruiz-Morales, J. Canales-Vázquez, J. Peña-Martínez, D. Marrero-López, J.T.S. Irvine, P. Núñez, J. Mater. Chem. 16 (2006) 540.
[153] Y.L. Zhang, S.W. Zha, M.L. Liu, Adv. Mater. 17 (4) (2005) 487.
[154] R.C. Schroden, A. Stein, in: F. Caruso (Ed.), 3D Ordered Macroporous Material, Colloids and Colloid Assemblies, Willey-VCH Verlag KgaA, Weinhein, Germany, 2004, pp. 465–493.
[155] D.G. Shchukin, A.A. Yaremchenko, M.G.S. Ferreira, V.V. Kharton, Chem. Mater. 17 (2005) 5124.
[156] A. Stein, Micropor. Mesopor. Mater. 44–45 (2001) 227.
[157] M.C. Carbajo, A. Gomez, M.J. Torralvo, E. Enciso, J. Mater. Chem. 12 (2002) 2740.
[158] M. Yano, A. Tomita, M. Sano, T. Hibino, Solid State Ionics 177 (2007) 3351.
[159] Z.P. Shao, C. Kwak, S.M. Haile, Solid State Ionics 175 (2004) 39.
[160] Z.P. Shao, J. Mederos, W.C. Chueh, S.M. Haile, J. Power Sources 162 (2006) 589.
[161] C.M. Zhang, Y. Zheng, R. Ran, Z.P. Shao, W.Q. Jin, N.P. Xu, J. Ahn, J. Power Sources 179 (2008) 640.
[162] F.S. Baumann, Ph.D. thesis, Oxygen reduction kinetics on mixed conducting SOFC Model Cathodes, Max Planck Institute for Solid State Research, Stuttgart, Germany, 2006.
[163] S. McIntosh, J.F. Vente, W.G. Haije, D.H.A. Blank, H.J.M. Bouwmeester, Chem. Mater. 18 (2006) 2187.
[164] D.Y. Wang, J. Electrochem. Soc. 137 (1990) 3660.
[165] F.S. Baumann, J. Fleig, H.-U. Habermeier, J. Maier, Solid State Ionics 177 (2006) 3187.
[166] F.S. Baumann, J. Fleig, H.-U. Habermeier, J. Maier, Solid State Ionics 177 (2006) 1071.
[167] J. Maier, Physical Chemistry of Ionic Materials, John Wiley and Sons, Ltd., Chichester, England, 2004.
[168] E. Bucher, A. Egger, P. Ried, W. Sitte, P. Holtappels, Solid State Ionics 179 (2008) 1032.
[169] P.J. Gellings, H.J.M. Bouwmeester (Eds.), The CRC Handbook of Solid State Electrochemistry, CRC Press, 1997.
[170] B.C.H. Steele, Solid State Ionics 86–88 (1996) 1223.
[171] J. Fleig, J. Maier, J. Eur. Ceram. Soc. 24 (2004) 1343.
[172] J.M. Serra, V.B. Vert, M. Betz, V.A.C. Haanappel, W.A. Meulenberg, F. Tietz, J. Electrochem. Soc. 155 (2008) B207.
[173] D. Beckel, Ph.D. thesis, Thin Film Cathodes for Micro Solid Oxide Fuel Cells, ETH, Zürich, 2007.
[174] Z.V. Marinković, L. Mančić, J.-F. Cribier, S. Ohara, T. Fukui, O. Milošević, Mater. Sci. Eng. A 375–377 (2004) 615.
[175] C.R. Xia, W. Rauch, F.L. Chen, M.L. Liu, Solid State Ionics 149 (2002) 11.
[176] A. Esquirol, J. Kilner, N. Brandon, Solid State Ionics 175 (2004) 63.
[177] B. Wei, Z. Lü, X. Huang, S. Li, G. Ai, Z. Liu, W. Su, Mater. Lett. 60 (2006) 3642.
[178] S. Li, Z. Lü, B. Wei, X. Huang, J. Miao, Z. Liu, W. Su, J. Alloys Compd. 448 (2008) 116.
[179] B. Liu, Y. Zhang, L. Zhang, J. Power Sources 175 (2008) 189.
[180] B. Lin, H. Ding, Y. Dong, S. Wang, X. Zhang, D. Fang, G. Meng, J. Power Sources 168 (2009) 58.
[181] F.S. Baumann, J. Maier, J. Fleig, Solid State Ionics 179 (2008) 1198.

[182] P. Zeng, Z. Chen, W. Zhou, H.X. Gu, Z.P. Shao, S.M. Liu, J. Membr. Sci. 291 (2007) 148.
[183] G.Ch. Kostogloudis, Ch. Ftikos, Solid State Ionics 126 (1999) 143–151.
[184] K.K. Hansen, K. Vels Hansen, Solid State Ionics 178 (2007) 1379.
[185] A. Mineshige, J. Izutsu, M. Nakamura, K. Nigaki, J. Abe, M. Kobune, S. Fujii, T. Yazawa, Solid State Ionics 176 (2005) 1145–1149.
[186] R. Doshi, V.L. Richard, J.D. Carter, X.P. Wang, M. Krumpelt, J. Electrochem. Soc. 146 (1999) 1273–1278.
[187] W. Zhou, R. Ran, Z.P. Shao, W. Zhuang, J. Jia, H.X. Gu, W.Q. Jin, N.P. Xu, Acta Mater. 56 (2008) 2687.
[188] L. Ge, R. Ran, K. Zhang, S.M. Liu, Z.P. Shao, J. Membr. Sci. 318 (2008) 182.
[189] W. Zhou, Z.P. Shao, R. Ran, P.Y. Zeng, H.X. Gu, W.Q. Jin, N.P. Xu, J. Power Sources 168 (2007) 330.
[190] V.V. Kharton, F.M. Figueiredo, A.V. Kovalevsky, A.P. Viskup, E.N. Naumovich, A.A. Yaremchenko, I.A. Bashmakov, F.M.B. Marques, J. Eur. Ceram. Soc. 21 (2001) 2301.
[191] W.X. Zhu, Z. Lü, S. Li, B. Wei, J. Miao, X. Huang, K. Chen, N. Ai, W. Su, J. Alloys Compd. 465 (2008) 274.
[192] M. Yang, M. Zhang, A.Y. Yan, X.L. Yue, Z.F. Hou, Y.L. Dong, M.J. Cheng, J. Power Sources 185 (2008) 784.
[193] W. Zhou, R. Ran, Z.P. Shao, R. Cai, W.Q. Jin, N.P. Xu, J. Ahn, Electrochim. Acta 53 (2008) 4370.
[194] R.A. Outlaw, S.N. Sankaran, G.B. Hoflund, M.R. Davidson, J. Mater. Res. 3 (1988) 1378.
[195] Y. Wang, S. Wang, Z. Wang, T. Wen, Z. Wen, J. Alloys Compd. 428 (2007) 286.
[196] W. Zhou, Z.P. Shao, R. Ran, Z.H. Chen, P.Y. Zeng, H.X. Gu, W.Q. Jin, N.P. Xu, Electrochim. Acta 52 (2007) 6297.
[197] S.P. Jiang, J.G. Love, L. Apateanu, Solid State Ionics 160 (2003) 15.
[198] Y.B. Zhou, W. Zhou, R. Ran, Z.P. Shao, unpublished.
[199] B. Wei, Z. Lü, S. Li, Y. Liu, K. Liu, W.H. Su, Electrochem. Solid-State Lett. 8 (2005) A428.
[200] D. Kek, P. Panjan, E. Wanzenberg, J. Eur. Ceram. Soc. 21 (2001) 1861.
[201] M. Mori, N.M. Sammes, Solid State Ionics 146 (2000) 301.
[202] W. Zhou, R. Ran, Z.P. Shao, W.Q. Jin, N.P. Xu, J. Power Sources 182 (2008) 24.
[203] L. Ge, W. Zhou, R. Ran, S.M. Liu, Z.P. Shao, W.Q. Jin, N.P. Xu, J. Membr. Sci. 306 (2007) 318.
[204] S. Li, Z. Lü, X. Huang, B. Wei, W. Su, Solid State Ionics 178 (2007) 417.
[205] S. Li, Z. Lü, N. Ai, K. Chen, W. Su, J. Power Sources 165 (2007) 97.
[206] S. Li, Z. Lü, X. Huang, W. Su, Solid State Ionics 178 (2008) 1853.
[207] S. Li, Z. Lü, X. Huang, B. Wei, W. Su, J. Phys. Chem. Solid 68 (2007) 1707.
[208] H. Zhao, D. Teng, X. Zhang, C. Zhang, X. Li, J. Power Sources 186 (2009) 305–310.
[209] J. Ovenstone, J.-I. Jung, J.S. White, D.D. Edwards, S.T. Misture, J. Solid State Chem. 181 (2008) 576.
[210] H.H. Wang, C. Tablet, A. Feldhoff, J. Caro, Adv. Mater. 17 (2005) 1785.
[211] B. Wei, Z. Lü, X. Huang, M. Liu, N. Li, W. Su, J. Power Sources 176 (2008) 1.
[212] M. Arnold, H. Wang, A. Feldhoff, J. Membr. Sci. 293 (2007) 44.
[213] W. Zhou, R. Ran, R. Cai, Z.P. Shao, W.Q. Jin, N.P. Xu, J. Power Sources 186 (2009) 244–251.
[214] E. Bucher, A. Egger, G.B. Caraman, W. Sitte, J. Electrochem. Soc. 155 (2008) B1218.
[215] A. Yan, M. Cheng, Y. Dong, W. Yang, V. Maragou, S. Song, P. Tsiakaras, Appl. Catal. B 66 (2006) 64.
[216] A. Yan, V. Maragou, A. Arico, M. Cheng, P. Tsiakaras, Appl. Catal. B 76 (2007) 320.
[217] A. Yan, M. Yang, Z. Hou, Y. Dong, M. Cheng, J. Power Sources 185 (2008) 76.
[218] A. Yan, B. Liu, Y. Dong, Z. Tian, D. Wang, M. Cheng, Appl. Catal. B 80 (2008) 24.
[219] S. Švarcová, K. Wiik, J. Tolchard, H.J.M. Bouwmeester, T. Grande, Solid State Ionics 178 (2008) 1787–1791.